Analysis and modeling of calendar aging of a commercial LiFePO$_4$/graphite cell

Maik Naumann*, Michael Schimpe, Peter Keil, Holger C. Hesse, Andreas Jossen

Institute for Electrical Energy Storage Technology (EES), Technical University of Munich (TUM), Arcisstraße 21, 80333 Munich, Germany

ABSTRACT

This paper presents a comprehensive calendar aging study on a lithium-ion battery with a test duration of 29 months. This aging study was realized with a widely used commercial LiFePO$_4$/graphite cell from *Sony/Murata*, which promises both long calendar and cycle lifetime, which is especially required for stationary battery applications. The development of the cells' capacity, as well as the resistances, are shown in a static calendar aging study for 17 test points, each with 3 cells, having constant storage conditions of temperature and state of charge. Based on the measurement data, a semi-empirical aging model is presented for the capacity loss and resistance increase, consisting of only 5 parameters which are valid for all storage conditions. An additional dynamic calendar aging study is performed with 9 months test duration for model validation, consisting of 15 test points with varying conditions of temperature and state of charge. The absolute model errors against the validation data points remain below 2.2% for the capacity loss and below 6.9% for the resistance increase for all dynamic validation tests. In conclusion, this calendar aging model allows the prognosis of the calendar lifetime of LiFePO$_4$/graphite batteries in different applications with varying storage conditions over time.

© 2018 Elsevier Ltd. All rights reserved.

1. Introduction

1.1. Motivation

With decreasing battery prices and the growth of the renewable energy share in the last years, stationary applications for lithium-ion batteries have evolved rapidly along with the existing and also emerging portable applications and electric vehicles (EVs). In portable and EV applications the batteries' energy density is one of the most important technical parameters for the choice of technology and system design. In contrast, for stationary applications, the economic value of a battery energy storage system (BESS) is primarily assessed when designing these systems.

In addition to the investment price of the battery system, the achievable lifetime is a crucial parameter for the profitability of BESS due to the long system lifetime of up to 20 years required [1]. As current mass-produced LiFePO$_4$/graphite (lithium iron phosphate (LFP)/C) battery cells show cycle stability up to 10,000 full equivalent cycles (FECs) until the capacity underruns 80% of the original capacity [2,3], the cycle lifetime is commonly not a

limiting factor in stationary applications: Within a operation of 20 years, only about 6000 FECs are expected for home energy storage [1] and no more than about 10,000 FECs for primary frequency regulation [4,5]. The total aging result is a combination of calendar and cycle aging when the superposition model of lithium-ion battery aging [6] is applied. Consequently, the overall contribution of calendar aging is dominant for battery cells with high cycle life. Thus, the calendar lifetime of lithium-ion battery cells with a high cycle life becomes a decisive parameter, which has to be estimated precisely when assessing the influence of battery lifetime on the profitability in stationary battery applications.

This paper shows a comprehensive calendar aging study with 885 days of storage test duration, which is used to develop an aging model enabling the estimation of resulting battery lifetime under different storage conditions of temperature and state of charge (SOC). All experiments are performed with a commercial 3 Ah 26650 LFP/C cell (see Section 2.1). This *Sony/Murata* LFP/C cell is used under the brand name *fortelion* in many commercial home energy storage systems. Furthermore, this LFP/C cell is used in the 192 kWh battery energy storage system in a container format, named *Energy Neighbor* [7,8], which was developed together with *VARTA Storage GmbH* and *ZAE Bayern* and is under investigation in the project *EEBatt* [9].

Although the fact that this cell is widely used in stationary applications, the authors are not aware of publications where the

---

* Corresponding author.
   E-mail address: maik.naumann@tum.de (M. Naumann).
   URL: http://www.ees.ei.tum.de/en/ (M. Naumann).

Acronyms

BESS   battery energy storage system
BOL   begin of life
CC   constant-current
CM   capacity measurement
CTS   cell test system
CU   check-up
CV   constant-voltage
DOC   depth of cycle
DVA   differential voltage analysis
EIS   electrochemical impedance spectroscopy
EOL   end of life
EOT   end of test
EV   electric vehicle
FEC   full equivalent cycle
LAM   loss of active material
LFP   lithium iron phosphate
LLI   loss of lithium inventory
OCV   open circuit voltage
SEI   solid electrolyte interphase
SOC   state of charge
SOH   state of health
TP   test point

aging of this cell is investigated or appropriate aging models are presented. Only Lepiorz [10] examined the aging effects of this cell during operation, however, the focus of his work was the path dependance of the aging rate when applying dynamic load profiles.

There is plenty of literature on calendar aging and corresponding lifetime models for various lithium-ion batteries and especially for LFP/C cells, which serve as the basis for this paper and are presented in the following section.

1.2. Literature review

The review paper of Barré et al. [11] on battery aging mechanisms emphasizes that the growth of the solid electrolyte interphase (SEI) on the graphite anode is by far the most prominent aging mechanism that occurs when lithium-ion battery cells are stored in an experimental setup. The SEI growth leads to an irreversible loss of lithium inventory (LLI) (i.e. loss of cyclable lithium) as well as an increase of cell's impedances and is accelerated with increased temperatures and higher SOCs. Additional capacity fade could occur due to the loss of active material (LAM) on the cathode and anode. Li et al. [12] showed for a commercial LFP/C cell an accelerated growth of the SEI (LLI) and additionally a blocking mechanisms of graphene layers of the anode (LAM) during cycle operation at high temperatures of 60 °C. They demonstrate that this LAM mechanism of the anode is mainly caused by Fe that dissolves from the cathode and is deposited on the graphite surface in cycle operation. Furthermore, Li et al. [13] showed this effect also in a calendar aging study for the same LFP/C cell, however this LAM of the anode occurs mainly at high storage temperatures (60 °C) and is almost negligible at moderate temperatures. Hence, the LLI by SEI growth dominates for different cell types when exposed only to calendar aging as shown by Keil et al. [14]. Thereby calendar aging results in capacity fade and resistance increase of the cell, reducing the maximum available power and energetic efficiency.

Alongside, there are effects that could lead to an increase of the available capacity when performing capacity measurements with several cycles: Gyenes et al. [15] originated this capacity increase

for a $LiNiMnCoO_2/C$ cell with the fact that lithium atoms are stored in the anode overhang areas, which is the portion of the anode that extends past the cathode electrode of commercial lithium-ion cells. The lithium atoms stored in the anode overhang areas can be recovered by performing several full cycles. Furthermore, Gyenes et al. showed that this capacity recovery effect depends strongly on the preceding storage SOC. Lewerenz et al. [16,17] and Wilhelm et al. [18] investigated the same effect for LFP/C cells and stated additionally, that the recoverable capacity depends on the size of the overhang area. Wilhelm et al. quantified the anode overhang area with about 10% in a commercial 18,650 cell and measured a maximal capacity difference of 3.6% between cells stored at a low and high storage SOC by this effect. An important conclusion is the fact, that the possible capacity recovery due to the anode overhang areas has to be considered when assessing the state of health of battery cells.

The following Table 1 shows a selection of different calendar aging studies. The studies are classified into the different existing aging model types that have been applied to simulate the aging behavior: Empirical, Semi-empirical and Physico-chemical. Some papers show experimental aging data without presenting models for lifetime predictions (see the first row). As LFP/C cell calendar aging is in the focus of this paper, the literature was additionally classified into LFP/C and other cell types. All mentioned calendar aging studies investigate the influence of both, temperature and SOC, by applying several storage conditions with different temperatures and SOCs of the stored cells. Most of the presented aging models are able to validate the measured capacity fade under constant storage conditions with acceptable prediction errors. Only a few of the studies also demonstrate models predicting the resistance increase [23,28,6], and only Prada et al. [39] evaluates the investigated resistance increase with an aging model for LFP/C cells.

Most of the calendar aging studies show non-linear trends of the capacity fade for different storage temperatures and SOC. In contrast, in the aging study of Lewerenz et al. [16,41] the capacity fade follows a linear trend at moderate storage temperatures, but at 60 °C a non-linear trend is shown for different storage SOC. Hence, they state that the capacity aging trends are path-invariant for temperatures lower than 45 °C and path-depending for temperatures higher than 50 °C. Furthermore, it could be concluded that the widely observed square root dependance over time of the capacity fade is possibly connected with the reversible capacity effect of the anode overhang areas as explained above. Then, the measured capacity fade would be accelerated by a reversible lithium flow into the anode overhang areas dependent on the storage SOC at the begin of a calendar aging study and slow down when the overhang areas are filled up. Even so, it remains unclear how to consider this effect correctly when developing calendar aging models, since the capacity trapped in the anode overhang areas can be recovered only by storing the cells at a low SOC for several days or performing several full cycles before every capacity measurement (CM), leading to an additional cycle aging effect. Furthermore, due to the different positions and distances to the cathode counterpart, the time constants of this lithium flow/capacity recovery are diverse for the different positions of the

Table 1
Overview of lithium-ion battery calendar aging literature classified into different aging models and cell types.

Aging model type	LFP/C	Other cell types
None (tests only)	[13,14,16,19–21]	[14,19,22–24]
Empirical	[10,25–27]	[28,29]
Semi-empirical	[30,31]	[6,31–35]
Physico-chemical	[36–39]	[40]

anode overhang areas, which implies the application of comprehensive physico-chemical models.

In fact, aging models should also be used for the simulation of dynamically changing cell storage conditions when estimating, for instance, the battery lifetime of a stationary application. Therefore, it is necessary to understand and correctly apply the path dependance of calendar aging when aging models are used in simulations with dynamic profiles of temperature and SOC. However, only the following studies on LFP/C calendar aging validate the respective aging models with dynamic storage conditions by alternating the temperature but only at a constant SOC [16,25,30,31,39]. Only Sarasketa-Zabala et al. [25] present a validation with alternating temperatures at different SOC with a relatively long experiment period of about 650 days. In contrast, in this paper additional model precision is obtained by:

1 Investigating multiple cells per storage condition to reduce thereby possible deviations in the aging behavior due to cell-to-cell parameter variations.
2 Examining different combinations of dynamically changing storage conditions.
3 Applying an aging model that uses the same set of parameters for every storage condition.

Although the aging model of Sarasketa-Zabala et al. shows predictions errors <1%, the model cannot be adapted to estimate the aging of further LFP/C cells due to the missing parameter fitting procedure and lack of customizable physico-chemical parameters.

There are further aging studies on path dependance of lithium-ion battery aging [28,42–44]. However, only Su et al. [29] investigate the pure calendar aging under static and alternating (non-static) storage conditions of both, temperature and SOC, for a $LiNiMnCoO_2$/C cell. Additionally, they develop an empirical aging model based on the static aging study and validate it with the measurement data from the non-static aging study. Our additional dynamic calendar aging study is designed similarly. However, by using 2 cells for each changing storage condition with switched order over time, we are able to understand the path dependance of calendar aging systematically for different storage conditions of temperature and SOC.

In conclusion various authors have investigated the specific aging effects relevant of LFP/C calendar aging. With this study we combine these aspects and present an aging model based on a long-lasting experiment with numerous storage conditions for both, temperature and SOC. Furthermore this aging model is validated systemically with dynamically changing storage conditions. However, this calendar aging model applies only for one single cell. Considering a BESS consisting of many serial and parallel connected cells, the possible cell-to-cell parameter variation [45] and inhomogeneous temperature or SOC distribution [46] could lead to deviating operation conditions and hence to a deviating aging of the single cells [47]. Then, in a BESS simulation the influence of the deviating capacity decrease and resistance increase due to calendar and cycle aging of each cell has to be considered. In case that all cells in a battery system would have the very same cell parameter values and operation conditions, the BESS capacity degradation and resistance increase can be estimated with the calendar aging of one single cell.

1.3. Paper highlights

In this paper we present the first, and at the same time very comprehensive, calendar aging study for a widely commercially used LFP/C cell (see Section 2.1). We investigate 17 test points (TPs) in a static calendar aging study, each with 3 cells, for constant storage conditions at various temperatures, as well as SOCs and

having an experiment duration of over 885 days. Then 15 TPs are examined in a dynamic calendar aging study, in total 15 cells, with alternating conditions of temperature and SOC. These TPs are used later for the validation of the aging model derived from the static calendar aging study. First, the experimental data from the static calendar aging study are analyzed in order to verify the measurements and to explain the aging effects. Then a semi-empirical aging model is developed and finally validated with data from the TPs with dynamic storage conditions. Conclusions for the design and possible acceleration of further calendar aging studies are derived from this study. This calendar aging model together with an cyclical aging model is going to be used in the techno-economic simulation of stationary BESS in a future publication.

1.4. Paper content and structure

First, the experimental setup and the applied measurement methods of the calendar aging studies are described in Section 2. Then in Section 3 the aging data is presented and verified. Afterwards, a semi-empirical calendar aging model is derived and validated with the data from the dynamic calendar aging study TPs. The results of the calendar aging studies, the aging model development, and the model validation with the dynamic calendar aging study are summarized in Section 4. Finally, in Section 5 an outlook of the next steps is given regarding the development of an complete aging model, where the calendar aging model presented here will be integrated.

2. Experimental

In this section the experimental setup of the calendar aging study will be given. First, the investigated cell is presented. Thereafter, the single measurement procedures are shown and followed by the description of the testing procedures applied in both aging studies. Finally, the design of the experiments of both the static calendar aging study and the dynamic calendar aging study is explained. Having defined the TPs within the design of experiment, the selection procedure of the cells needed for these studies from many cells is shown.

2.1. Investigated cell

In this calendar aging study we investigate a commercially available 3 Ah 26,650 LFP/C cell from *Sony* named *US26650FTC1*. Table 2 shows the most important cell parameter values from the manufacturer's datasheet. In the cell's datasheet the rated capacity is defined with 2.85 Ah. However, Rumpf et al. measured in [45] over 1100 cells out of two batches before this aging study and the mean discharge capacity resulted in 3.019 Ah. In this preceding CM we applied a full charge and discharge cycle with constant currents of 3.0 A followed by constant-voltage (CV)-phase (CV until $I_{disch, CV} < C/20 = 150$ mA).

Consequently we use 3.0 A and thereby 1 C as the maximum continuous charge current in the measurements of this aging study. Other aging studies applied C-rates lower than 1 C in the CM [14], however, we apply 1 C in order to minimize the duration of the check-up (CU). Furthermore, by discharging with a lower current with exemplary 0.2 C only about 1.4% of the nominal capacity can be extract additionally in the constant-current (CC)-phase. By combining a 1 C CC discharge with a CV-phase, the effect of the absolute current on the extractable capacity is remarkably reduced.

Before this initial CM, all cells were delivered and stored at 50% SOC at about 8 °C to minimize the inevitable calendar aging. Hence, we assume that all cells should have almost the same useable capacity at the beginning of the aging study without increased or

Table 2
Datasheet parameters of the investigated LiFePO$_4$/graphite cell Sony US26650FTC1.

Parameter	Value	Notes
Nominal capacity	2.850 Ah / 3.000 Ah	Datasheet capacity/measured cell capacity in this study
Nominal voltage	3.2 V	
Max. charge voltage	3.65 V / 3.6 V	Datasheet definition/voltage applied in this study
Min. discharge voltage	2.00 V	
Ohmic impedance (1 kHz), AC	18 mΩ	
Max. continuous charge current	2.85 A / 3.00 A	Datasheet definition/current applied in this study
Max. continuous discharge current	20 A	
Temperature range charge	0 °C to 45 °C	Datasheet: Maximum surface temperature 60 °C
Temperature range discharge	−20 °C to 60 °C	Datasheet: Maximum surface temperature 80 °C
Mass	84.5 g	

decreased capacity differences due to possible effect of the anode overhang areas. In order to assess the possible influence of the anode overhang area, one sample cell was opened at begin of life (BOL) and measured: The total coated area of the jelly roll's anode is 150.2 × 5.7 cm^2 top side and 142.1 × 5.7 cm^2 bottom side. The overhang areas are separately shown in Table 3 for the different positions on the anode and represent in sum 88.46 cm^2. Hence, the anode overhang areas correspond together to 6.2% of the total coated area of the anode. Wilhelm et al. [18] measured about 10% anode overhang and observed a maximal decrease of the capacity difference of 3.6% of the nominal capacity between cells stored for months at a low and high SOC by recovering the capacity of the anode overhang areas. By transferring these results on the here investigated cell, about 2.2% of the nominal capacity would be the maximal recoverable capacity between cells stored a low and high SOC. However, only by storing the cells at a low SOC for several days or performing several full cycles before every CM (leading to an additional cycle aging effect) could recover most of the capacity of the anode overhang areas. Though, this is in conflict with the concept of a calendar aging study where the cycle operation should be kept to a minimum. In this aging study, the capacity measurements are performed with two consecutive full cycles in order to minimize the cycle aging and the influence of the preceding storage SOC due to the possible recovery effect of the anode overhang area. Hereby, for all TPs the second cycle capacity does not exceed 0.4% of the first cycle capacity during the CM of the whole aging study. Only for the test points with a storage SOC of 0% the second full cycle show less capacity than the first cycle during the CM of the whole aging study. Furthermore, after the initial CM only 2 out of the 17 TPs with different storage temperatures and SOC of this calendar aging study showed a slight capacity increase during the first CM. By using the average capacity of two consecutive full cycles during the CM the trend of the capacity recovery effect is considered at least in the results of this calendar aging study. In order to evaluate the influence of the anode overhang area more in detail during the whole aging study, Lewerenz et al. [48] suggest the capacity difference analysis (CDA) to compare the extractable capacities with different C-rates. However, in this aging study we performed the periodic CU with only one C-rate and applied a lower C-rate only in four

measurements distributed over the whole aging study, which are evaluated with the differential voltage analysis (DVA) in Section 3.1.2. In conclusion, the anode overhang areas influence the measurable capacity dependent on the preceding storage condition in addition to the capacity loss due to calendar aging. However, we consider this capacity effect of the anode overhang areas as a theoretical capacity influence factor, since the impact of this effect was hard to determine accurately during this calendar aging study. In addition, the absolute influence is estimated to be quite little in comparison to the influence of the temperature and SOC on the resulting calendar aging. Furthermore, the scope of this paper is to develop a lifetime model for BESS simulations with dynamic battery operation. Hence, the fade of the useable capacity and the decrease of the performance dependent in certain temperature and SOC ranges is required.

2.2. Measurement equipment

The CMs were performed with two BaSyTec cell test systems (CTSs), each with 32 channels, and an Espec LU-123 climate chamber at $T = 25$ °C. The surface temperature of each cell was monitored using NTC thermistors. To perform electrochemical impedance spectroscopy (EIS) measurements we used a BioLogic VMP3 potentiostat with 16 channels and a climate chamber at $T = 25$ °C.

2.3. Measurement procedures

Two different measurement procedures were applied: Standard CU and extended CU. The standard CU consists of a CM and is followed by an EIS measurement. The extended CU is principally the same as the standard CU, but between the CM and EIS, a low rate charge and discharge measurement is performed. Both procedures involve the following CM test plan at 25 °C:

1 Initial discharge: CCCV protocol to 2.0 V using a CC $I_{disch,CC} = 1$ C = 3A followed by a CV-phase until $I_{disch,CV} <$ C/20 = 150 mA. 25 min relaxation pause.
2 Two consecutive full cycles:
Full charge: CCCV protocol to 3.6 V using a CC $I_{ch,CC} = 1$ C = 3A followed by a CV until $I_{ch,CV} <$ C/30 = 100 mA. 25 min relaxation pause.
Full discharge: CCCV protocol to 2.0 V using a CC $I_{disch,CC} = 1$ C = 3A followed by a CV-phase until $I_{disch,CV} <$ C/20 = 150 mA. 25 min relaxation pause.
3 SOC adjust: Charging with $I_{ch,CC} = 1$ C = 3A until reaching 50% SOC by Ah-counting related to the mean value of the actual capacity measured in the two full discharge steps. 25 min relaxation pause.
4 Pulses: 1/3 C discharge pulse for 10 s, 10 min relaxation, 1/3 C charge pulse. 10 min relaxation. Afterward, the same pulse procedure is applied with 2/3 C and 1 C.

Table 3
Anode overhang areas: Position and areas

Anode position	Area: width × height
Start top side	1.3 × 5.7 cm^2
Start bottom side	1.9 × 5.7 cm^2
Middle top side	2.0 × 5.7 cm^2
Middle bottom side	2.0 × 5.7 cm^2
End top side	4.6 × 5.7 cm^2
End bottom side	1.2 × 5.7 cm^2
Edges top side	143.6 × 0.1 cm^2
Edges bottom side	143.6 × 0.1 cm^2

In this CM, the capacity is determined by performing two consecutive full cycles in order to minimize the influence of the possible recovery effect due to the anode overhang. Furthermore, both full cycles are performed with CV-phases in the charge and also in the discharge direction aiming to obtain all the available capacity. Thereby, the discharge CV-phases last on average 285 s for the first cycle and 272 s for the second cycle resulting in about 2.4% and 2.2% of the total capacity at BOL in the respective cycle.

After the CM a 12 h relaxation pause is applied to await that the cell internal relaxation processes have declined sufficiently [49]. The following EIS measurement records the cell impedance within a logarithmically spaced frequency range $f \in [10, 000, 0.01]$ Hz using an excitation current amplitude of $\hat{I} = 100$ mA. The number of frequencies per decade (fpd) and number of measures per frequency (mpf) changes according to the consecutive sub-intervals: $f \in [10, 000, 1]$ Hz (13 fpd, 10 mpf), $f \in]1, 0.1]$ Hz (10 fpd, 5 mpf), $f \in]0.1, 0.01]$ Hz (3 fpd, 2 mpf). The EIS measurement is performed at $SOC = 50\%$ and $T = 25°C$.

Within the extended CU an additional low rate charge and discharge measurement is performed at 25 °C with the following test plan:

1. Full charge: CCCV protocol to 3.6 V using a CC $I_{ch,CC} = 1$ C = 3A followed by a CV until $I_{ch,CV} < C/200 = 15$ mA. No relaxation pause.
2. Slow discharge: CC to 2.0 V using a CC $I_{disch,CC} = 0.02$ C = 60 mA. No relaxation pause.
3. Slow charge: CC to 3.6 V using a CC $I_{ch,CC} = 0.02$ C = 60 mA. 25 min relaxation pause.
4. Full discharge: CCCV protocol to 2.0 V using a CC $I_{disch,CC} = 1$ C = 3A followed by a CV until $I_{disch,CV} < C/20 = 150$ mA. 25 min relaxation pause.
5. SOC adjust: CC using a CC $I_{ch,CC} = 1$ C = 3A until reaching 50% SOC by Ah-counting related to the actual capacity measured in the full discharge step.

The low rate charge and discharge measurements are used later for the DVA.

2.4. Testing procedure

Fig. 1 gives an overview of the testing procedure applied in this calendar aging study. For this aging study, 1100 fresh cells of two batches (batch 1: 600 cells, batch 2: 500 cells) were available and had been examined [45] with an initial reduced CU measurement. Then a selection procedure was applied for choosing the count of cells needed for both calendar aging studies (see Section 2.7). All cells were stored with a storage SOC of 50% at about 8 °C in order to minimize the inevitable calendar aging. About 139 days after the CU of the 1100 fresh cells, an initial extended CU was performed with all selected cells at the beginning of the calendar aging study. Thereby, the capacity of selected 66 cells decreased slightly by about 0.5–1.2% and 0.8% on average. After this and the following CUs, each cell was charged to the respective storage SOC as defined by the test matrix (see Table 4) by Ah-counting related to the actual capacity measured in the full discharge step of the prior CM. Thereafter all cells were stored at the temperature defined in the design of the experiments (see Sections 2.5 and 2.6). In order to measure the aging behavior as a function of time, the storage of cells had been interrupted after certain time periods to derive periodic CU measurements. Every CU measurement influences the calendar aging behavior of the investigated cells: The different storage SOC and temperature during the CU measurement results in a different calendar aging. For the TPs with temperatures >25 °C the aging speed is reduced and consequently increased for the TPs
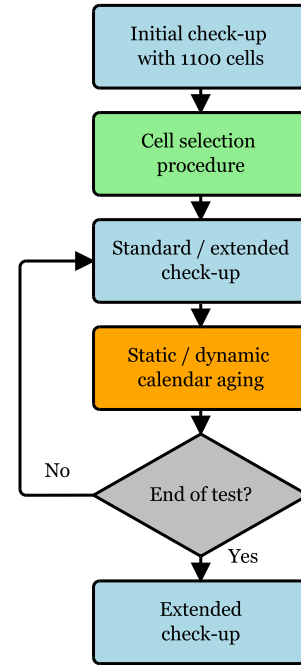

Fig. 1. Testing procedure of the calendar aging study.

Table 4
Test matrix of the static calendar aging study with the number of cells for each storage condition.

Temperature SOC	0 °C	10 °C	25 °C	40 °C	60 °C
0%			3	3	3
12.5%				3	
25%				3	
37.5%				3	
50%	3	3	3	3	3
62.5%				3	
75%				3	
87.5%				3	
100%			3	3	3

with temperatures <25 °C during the CU with a storage tempera- ture of about 25 °C. However, the CU measurements last in sum only about 0.9% of the total duration of this calendar aging study. Hence, the different calendar aging during the CU measurements can be neglected for the TPs with a storage temperature of ≥25 °C. For the TPs with the storage temperatures of 0 °C and 10 °C almost no aging is observable in comparison to the higher temperatures. However, by performing the CU measurements at 25 °C, higher calendar aging can be expected due to the influence of the elevated test temperature. In order to determine the true calendar aging at the storage temperature of 0 °C and 10 °C, the later developed calendar aging model could give an estimate for the influence of the CU measurements. Another strategy would have been the realization of these TPs with storage temperature of 0 °C and 10 °C with longer time intervals between the CU measurement in order to minimize the influence of the elevated test temperature. As a result, these TPs are not considered in the parametrization of the calendar aging model in Section 3.2. Additionally, about 3 FEC of each CM might lead to a small portion of cycle aging, however, in sum over the 35 CU measurements only 105 FEC are performed. By assuming a cycle stability of 10,000 until the capacity underruns 80% of the nominal capacity [2,3], the pure cycle aging would contribute to only about 0.21% capacity loss. Hence, we neglect the cycle aging influence of the CU on the calendar aging. At the

beginning of the study, the CU measurements were repeated every week for three periods, every 2 weeks for the next three periods and afterwards every 4 weeks. In the last quarter of the aging study, the CU measurements were carried out 2 times at 8 week intervals and continued with 6 week intervals until the end of the study. In total 35 CU of which 4 are extended CU measurements were performed during the aging study. The aging study was stopped (end of test (EOT)) after 970 days duration (885 days under storage conditions) and completed with a final extended CU measurement.

2.5. Static aging test points

Due to the fact that both this calendar aging study and the supplementary cycle aging study, relied on the same measurement equipment, the CU measurement of the calendar aging study had to be integrated into the test procedure of the cycle aging study. In order to minimize the break times of the cyclization realized with the CTSs, the CU measurement of the calendar aging study was integrated into the obligatory relaxation time between the CM and EIS measurements of the cycle aging study. Hence, the maximum count of cells under investigation was limited by the available 64 CTS channels.

We decided to use 3 cells each for every TP in order to reduce the influence of cell-to-cell parameter variation and therefore dependent possible deviations in the aging behavior and to reduce the danger of premature cell failures. Furthermore, neither published aging data nor experience derived from own measurements was available for the investigated cell in order to estimate the development of cell-to-cell variation during the aging study. Thus, originating from 64 available CTS channels, the number of TPs was limited to 17, because 9 channels had to be reserved for the CU measurements of some of the cycle aging TPs. Nonetheless, with 17 TPs it is possible to cover the whole SOC-range at different temperatures with adequate step sizes of both influence parameters. Furthermore, the calendar aging studies shown in Table 1 used less than 17 TPs. Only [14] performed a calendar aging study with more than 48 TPs, however, with only one cell each.

Although stationary BESS are designed to operate over more than 20 years, the experiment was naturally limited by time in addition to the limitations of the available measurement equipment. In order to reach the often used end of life (EOL) limit of state of health (SOH) <80% [6] during the limited time of this aging study, we decided to accelerate the aging by increasing the storage temperature. Assuming that the cell aging rate follows the exponential temperature influence given by the Arrhenius-law, the aging of TPs at higher temperatures can be used as a forecast for the TPs at lower temperatures. 60 °C was chosen as maximum TP temperature because the datasheet provides this as the maximum temperature for cell operation (see Table 2). Furthermore, it is not expected that battery cells are exposed to ambient conditions >60 °C in BESS applications. To prove the Arrhenius-law on the cell aging and to also test realistic storage conditions, TPs were also chosen at lower temperatures. Because almost no calendar aging effects are expected at temperatures lower than 0 °C, this temperature was set here as the lower limit. In accordance with the temperature range specified in the cell's datasheet, TP temperatures at 0 °C, 10 °C, 25 °C, 40 °C and 60 °C were chosen.

In stationary BESS applications, in most cases an air conditioning system is able to maintain the battery cells at optimal temperatures with respect to aging. A commonly used reference temperature is 25 °C since additional cooling leads to higher overall system efficiency losses. In order to achieve accelerated aging all relevant SOCs are tested at 40 °C, which is also the operation temperature of most of the TPs in the cycle aging study. To verify the Arrhenius-law here, one TP with 50% SOC is chosen at all temperatures. Furthermore, 50% is expected to be the average SOC in stationary BESS operation. In order to be able to assess the aging effects over the entire SOC-range, for the reference temperature of 25 °C and also for 60 °C, the SOC values 0% and 100% are added. At the main temperature of 40 °C, more SOC steps are necessary since nonlinear sensitivity could be expected. Hence, an evenly spaced graduation in 12.5% steps to reach exactly the middle SOC between the previous SOC of the TPs is applied. On the basis of this design of experiment, it should be possible to estimate the aging even for SOC not to be tested at other temperatures on the basis of the detailed SOC partition of the main temperature. From the previously described considerations, 17 TPs have been defined for the static calendar aging study and are shown in the TP matrix in Table 4. Each of the 17 TPs is covered with 3 cells.

2.6. Dynamic aging test points

The additional dynamic calendar aging study with alternating test conditions was motivated by the three following issues:

1 To validate the calendar aging model derived from the static calendar aging study.
2 To investigate the independence of the order of storage conditions.
3 To examine how the aging rate is influenced when changing storage SOC and/or temperature.

The main focus of this additional study was to validate the calendar aging models to be derived with measurements relying on different aging conditions. However, these measurements helped to develop the aging model by understanding the dependance of the order of storage conditions and the effect of switching between different conditions. Due to the fact that this dynamic aging study was started about 2 years after the start of the static aging study some of the results have been applied to design this experiment: The respective static parameter of each TP was chosen as maximum possible value, i.e. 100% SOC or 60 °C, to accelerate the aging effects. The experimental setup with 15 TPs with a total of 15 cells was then designed as shown in Table 5. Each TP is realized with one cell having one static and one dynamic condition (temperature or SOC). In order to investigate the independence of the order of storage conditions, one cell of each pair (e.g. TP1/TP2) is stored under the first given condition, the other cell of each pair on the second given conditions. Thereby, the dynamic condition of each cell is changed after a period of 4 weeks, when a CU measurement is performed. For instance, the cell of TP1 is stored at 100% SOC in the first interval at 25 °C and afterwards at 40 °C. The cell of TP2 is stored at 100% SOC but with the antithetic temperature order. In contrast, in the TP9-TP14 the temperatures are kept constant but the SOCs are changed after every storing period. The last TP15 is carried out with one cell stored constantly at 100% SOC and the temperature is changed dynamically after every storing period in this order: 60, 25, 40, 60, etc. °C.

Table 5
Test matrix of the dynamic calendar aging study with one cell for each test point.

Test point	Temperature	SOC
TP1/TP2	25/40 °C	100%
TP3/TP4	25/60 °C	100%
TP5/TP6	40/60 °C	100%
TP7/TP8	0/60 °C	100%
TP9/TP10	60 °C	0/50%
TP11/TP12	60 °C	0/100%
TP13/TP14	60 °C	50/100%
TP15	Dynamic	100%

2.7. Selection procedure

In order to select from the 1100 available cells a total of 66 cells, 51 for the static aging study and 15 for the dynamic aging study, a selection procedure was applied to obtain cells with preferably similar parameters to enhance the comparability between the cells:

1. Comparing the cell-to-cell parameter variation of batch 1 and 2, batch 1 with 600 cells showed a little less variation in most of the measured parameters and was therefore selected for the further steps.
2. Due to the fact that the various cell parameters do not correlate perfectly with each other [45], more than one parameter was necessary to consider in the selection procedure. Thus, we applied an algorithm that is able to select a defined count of cells by step-by-step choosing only those cells whose parameters are the closest to the mean values μ of every single parameter of the whole cell batch.

With this selection procedure 66 cells were selected. The selected cells' standard deviation σ of the discharge capacity C_{disch} decreased from $\sigma = 0.007$ Ah with a mean value of $\mu = 3.020$ Ah (batch of 600 cells) to $\sigma = 0.005$ Ah ($\mu = 3.018$ Ah). The standard deviation of the resistance $R_{DC,10s}$ decreased from $\sigma = 0.407$ mΩ ($\mu = 28.485$ mΩ) (batch of 600 cells) to $\sigma = 0.337$ mΩ ($\mu = 28.499$ mΩ).

3. Results and discussion

In this section, first of all the results of the calendar aging study are presented and primarily discussed. Afterward, the aging model is presented and validated.

Although a variety of parameters are available from the CU measurements, here we only evaluate the relative discharge capacity C_{disch} and relative resistance $R_{DC,10s}$ as they are the most representative parameters and commonly used in aging models for lifetime simulations. Later on, we also evaluate the low rate charge and discharge-curves measured in the extended CU and the impedance-spectra of the EIS measurement as part of every CU.

C_{disch} is determined as the mean of the entire discharge capacity (CC + CV-phase) in the two full cycles of the periodic CU (see Eq. (1)). $R_{DC,10s}$ is defined as the voltage difference measured between the beginning of relaxation after a constant current pulse $V(t = 0$ s$)$ and after 10 s of relaxation $V(t = 10$ s$)$ divided by the current of each pulse. Here, $R_{DC,10s}$ is calculated as the mean value of $R_{DC,10s}$ determined after a 1 C discharge pulse (disch) and 1 C charge pulse (ch) in the 4th phase of the CM during the periodic CU (see Eq. (2)).

$$C_{disch} = \frac{1}{2}(C_{CC_{1,disch}} + C_{CV_{1,disch}} + C_{CC_{2,disch}} + C_{CV_{2,disch}}) \quad (1)$$

$$R_{DC,10s} = \frac{1}{2}\left(\frac{V_{0s} - V_{10s}}{I_{disch}} + \frac{V_{0s} - V_{10s}}{I_{ch}}\right) \quad (2)$$

3.1. Aging results

3.1.1. Capacity and resistance measurements

In Fig. 2 the development of the relative discharge capacity C_{disch} and the relative resistance $R_{DC,10s}$ are shown for selected TPs at different temperatures and storage SOCs over the whole aging study with 35 CU measurements. All values are related to the measurements of the first CM. Since the cell-to-cell variation with identical storage conditions is minimal at BOL and even at EOL with $\Delta C_{disch} < 0.6\%$ and $\Delta R_{DC,10s} < 2.1\%$, only the mean value of the

three cells each with same storage condition, is shown in the following aging figures.

Fig. 2a and b shows the aging trend for different storage temperatures 0°C, 10°C, 25°C, 40°C, and 60°C at the storage $SOC = 0\%$, 50% and 100%. The capacity is decreasing for all temperatures over time, however, the rate of capacity decrease is slowing down over time as well. This capacity fade behavior was also shown in different publications [25,35] and modeled with a square root dependence over time. Ploehn et al. explained this square root dependance over time of the capacity fade with the growth rate of the SEI and their thickness. They state, that the SEI thickness increase leads to a decrease of the solvent diffusion rate and consequently to a slowing down of SEI growth rate and capacity loss. Further publications [37,50,51] stated similar concepts and approved their observations and models with measurements of the calendar aging of lithium-ion cells with graphite anodes.

For the aging trend of the capacity and the resistance, higher temperatures lead to higher rates of decrease or increase of both parameters respectively, however the relative resistance increase is almost double the relative capacity decrease for the respective TPs.

For the TP with 0% SOC at 25°C and 40°C the capacity increases slightly by maximum 0.22% in the first storage period probably due to the influence of the overhang areas but decreases afterwards. This capacity trend could be interpreted as a superposition of the capacity fade due to the aging by the SEI growth together with the limited capacity recovery from the anode overhang areas. It can be assumed that the same trend can not be observed for the TP with 0% SOC at 60 °C, because the capacity fade is probably stronger than the capacity recovery from the anode overhang areas. The resistance decreases for most of the TPs without a clear correlation to temperature or SOC at the beginning of the aging study by maximum 1.90% but increases thereafter for all temperatures, but in contrast to the capacity fade, the rate of resistance increase remains constant. The resistance decrease at the beginning could be explained by the possible influence of measurement uncertainties when measuring the resistance during the CM. Due to the fact, that the resistance changes are partly quite small at the beginning of the aging study for some TPs, small measurement errors at the first CM could lead to different trends in the subsequent CM. This inverse aging trend of the resistance at the beginning of aging study could be related as well to the effects of the anode overhang areas. However, the influence of the anode overhang areas on the resistance change remains unclear, because also the TPs in the middle SOC-range showed the same behavior as the TPs with very low and very high SOC, where the anode overhang effect could influence the capacity trends the strongest.

Between the CM of day 659 and 708 the capacity of the TP with 100% at 40°C decreases faster in comparison to the aging before and after this interval. Though, the interval between this CM and the preceding CM is with 50 days the first time during the aging study longer than the before performed interval of 27 days. However, the longer storage time is probably not the reason for this unique kink in the capacity loss of this TP, because the further TPs with 100% SOC at 25 °C and 60 °C show no similar trends.

The influence of storage SOC is shown in Fig. 2c and d at 40 °C for the storage SOCs from 0% to 100% for selected points in time from the beginning until the end of the aging study. The capacity decrease is stronger with higher SOCs. However, for the $SOC = 37.5 - 62.5\%$ there is almost no difference in the capacity fade observable for all shown points in time. Similar SOC behavior was shown by Keil et al. [14] for different lithium-ion cells with graphite anodes and explained with the stages in the graphite anode potential. In contrast, the resistance increase shows a non-monotonic dependance over the storage SOC with the highest
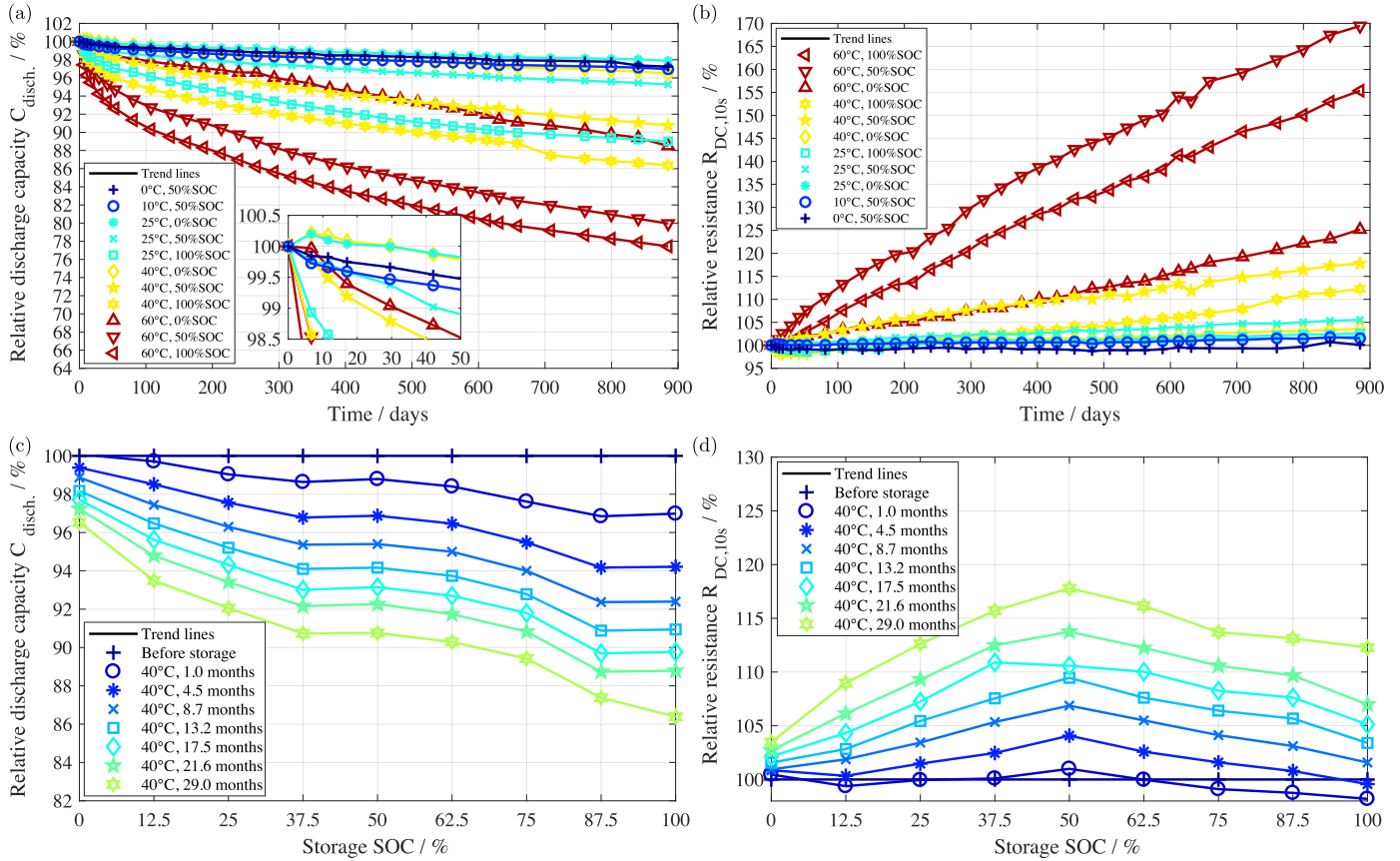
Fig. 2. Degradation over 885 days of selected TPs under different storage SOCs and temperatures: (a) Relative discharge capacity C_{disch} at SOC = 0%, 50% and 100% at 0 °C, 10 °C, 25 °C, 40 °C, and 60 °C. (b) Relative resistance $R_{DC,10s}$ at SOC = 0%, 50% and 100% at 0 °C, 10 °C, 25 °C, 40 °C, and 60 °C. (c) Relative discharge capacity C_{disch} at 40 °C at SOC = 0–100%. (d) Relative resistance $R_{DC,10s}$ at 40 °C at SOC = 0–100%. All values are related to the measurements of the first CM. Each subplot shows the mean values of the three cells of each TP. In subplot (a) the first 50 days are displayed enlarged in an extra view in order to see more details.

increase in the middle SOC-range. The evaluation of the EIS measurements in Table 6 show a similar behavior for the TPs with the storage temperature of 60 °C, since for all EIS-parameters the highest increase was observed for the test points with 50% SOC. However, for the further test points with 25 °C and 40 °C no clear trend of the impedance increase due to the storage SOC was seen. This influence of storage SOC on the resistance increase seems to be a special artifact of the investigated cell, because the authors are not aware of any publications where this behavior was observed. A possible explanation of this behavior could be the assumption, that the SEI grows homogeneously across the whole anode only when the cells are stored in the middle SOC-range where little capacity fade differences were observed over the storage SOC (see Fig. 2c). Outside this SOC-range towards 0% and 100% the SEI could grow inhomogeneously due to possible different lithiation and consequently voltage levels across the whole anode. Then, a homogeneous SEI would lead to relatively higher resistance increase than an inhomogeneous SEI, because the areas with less SEI thickness would dominate the measurable resistance. However, these assumptions remain to be proven by further experiments and post-mortem analysis of the investigated cell.

3.1.2. Differential voltage analysis

For a deeper understanding of the capacity fade Fig. 3 shows the DVA curves for selected TPs at different SOCs and temperatures. Thereby every subplot shows the dV/dQ-curve of only one of the three cells under the same storage conditions of each TP, because the averaged values of three cells of one TP would erase possible differences between the curves. The DVA was applied on the

discharge phase with 0.02 C in the low rate charge and discharge measurements in the 4 extended CU during the aging study (see Section 2.3) and is related to the work of Keil et al. [24]. In all dV/dQ-curves, the main peak in the DVA between 2.3 Ah and 2.5 Ah of the capacity results from a potential step, which indicates a different staging configuration of the intercalated lithium in the graphite-anode. Thereby, this main peak represents the single phase of LiC_{12} and is marked with circles in the respective color of each point in time. The area left and towards to this peak, corresponds to the transformation from LiC_{24} to LiC_{12} and the area right and away from the peak to the transformation of LiC_{12} to LiC_6. This peak divides the cell capacity C_{actual} into two characteristic capacities Q_1 and Q_2. Q_1 is the interval between 0% SOC and the main graphite peak, providing information about the capacity of the graphite anode. Q_2, is the interval between the main graphite peak and 100% SOC, providing information about the balancing of both electrodes. The sum of Q_1 and Q_2 is the respective remaining discharge capacity C_{actual} at each point in time of the shown TPs, which correlates with the capacity decrease shown in Fig. 2. Q_1 and Q_2 are defined graphically in Fig. 3a and are evaluated for all subplots in Fig. 4 as absolute values for better comparability. The TP with a storage SOC = 50% at 25 °C shows almost no variation of the dV/dQ-curves because the capacity decreased only about 4.7% during the 885 days of the aging study. Only a slight shift to the left is observable for the LiC_{12} peak, resulting in a decrease of Q_2 and nearly no change of Q_1. The TPs at the higher temperature of 60 °C show a stronger variation of the dV/dQ-curves, however only the LiC_{12} peak is shifting to the left and the other parts almost remain in the same position and shape. Consequently, we see in Fig. 4 a
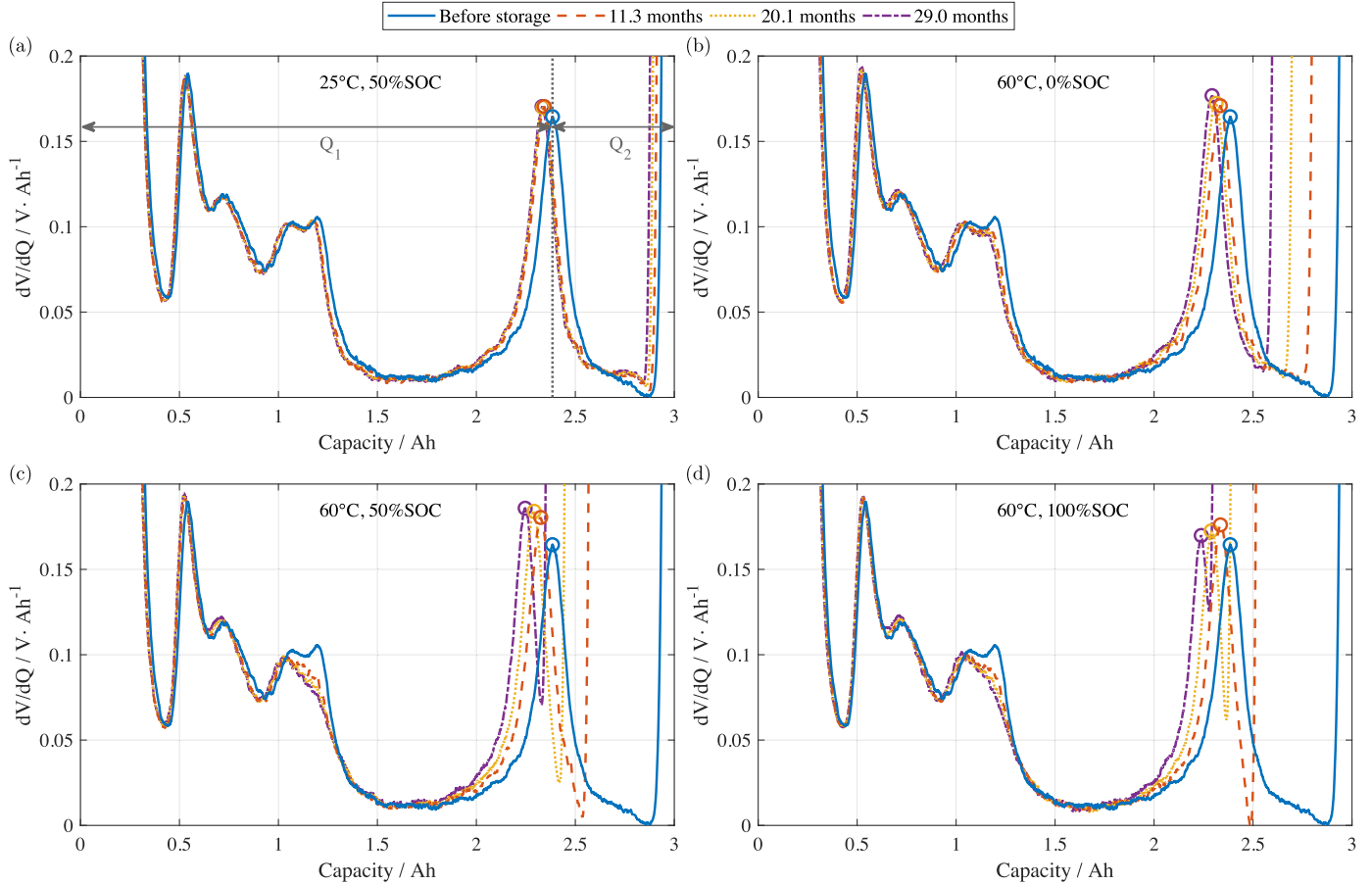
Fig. 3. DVA of selected TPs with different storage SOCs and temperatures at different points in time during the aging study: (a) At *SOC* = 50% at 25 °C. (b) At *SOC* = 0% at 60 °C. (c) At *SOC* = 50% at 60 °C. (d) At *SOC* = 100% at 60 °C. The circles show in each *dV/dQ*-curve the peak which is related to the single phase of LiC_{12} in the graphite-anode. The DVA is applied on the low rate discharge measurement described in Section 2.3.

decrease of both Q_1 and Q_2 of the TPs at the higher temperature of 60 °C. With higher storage SOCs Q_2 is decreasing stronger, but Q_1 is decreasing nearly constant for all SOCs. Since almost no decrease of Q_1 at 25 °C is observed, it can be assumed, that no LAM occurs and the capacity fade results solely from LLI for this test point. In contrast, a slight decrease of Q_1 is observable in the *dV/dQ*-curves at 60 °C. Hence, there might be some LAM of the negative electrode as already shown by Li et al. and Lewerenz et al. for LFP/C cells [13,52] at elevated temperatures caused by the deposition of Fe on the anode. However, LLI remains the dominating factor for capacity fade, which can be identified by the marked reductions in Q_2 for all

shown *dV/dQ*-curves. Due to the fact that the capacity fade correlates with the decrease of Q_2, the observed aging effects result mostly from the SEI growth on the graphite anode.

3.1.3. Electrochemical impedance spectroscopy

The EIS-curves in Fig. 5 give an insight into the development of the impedances for selected TPs at different SOCs and temperatures at selected points in time during the aging study. Thereby every subplot shows the EIS-curve of only one of the three cells under the same storage conditions of each TP, because the averaged values of three cells of one TP would impede the comparability of the curves.

The EIS measurement conditions are described in detail in Section 2.3. In all EIS subplots the following parameters are labeled respectively with markers:

Fig. 4. Development of the Q_1 and Q_2 parameters of the *dV/dQ*-curves shown in Fig. 3.

Table 6
Relative change of EIS-parameters from the beginning until the end of the aging study for selected TPs.

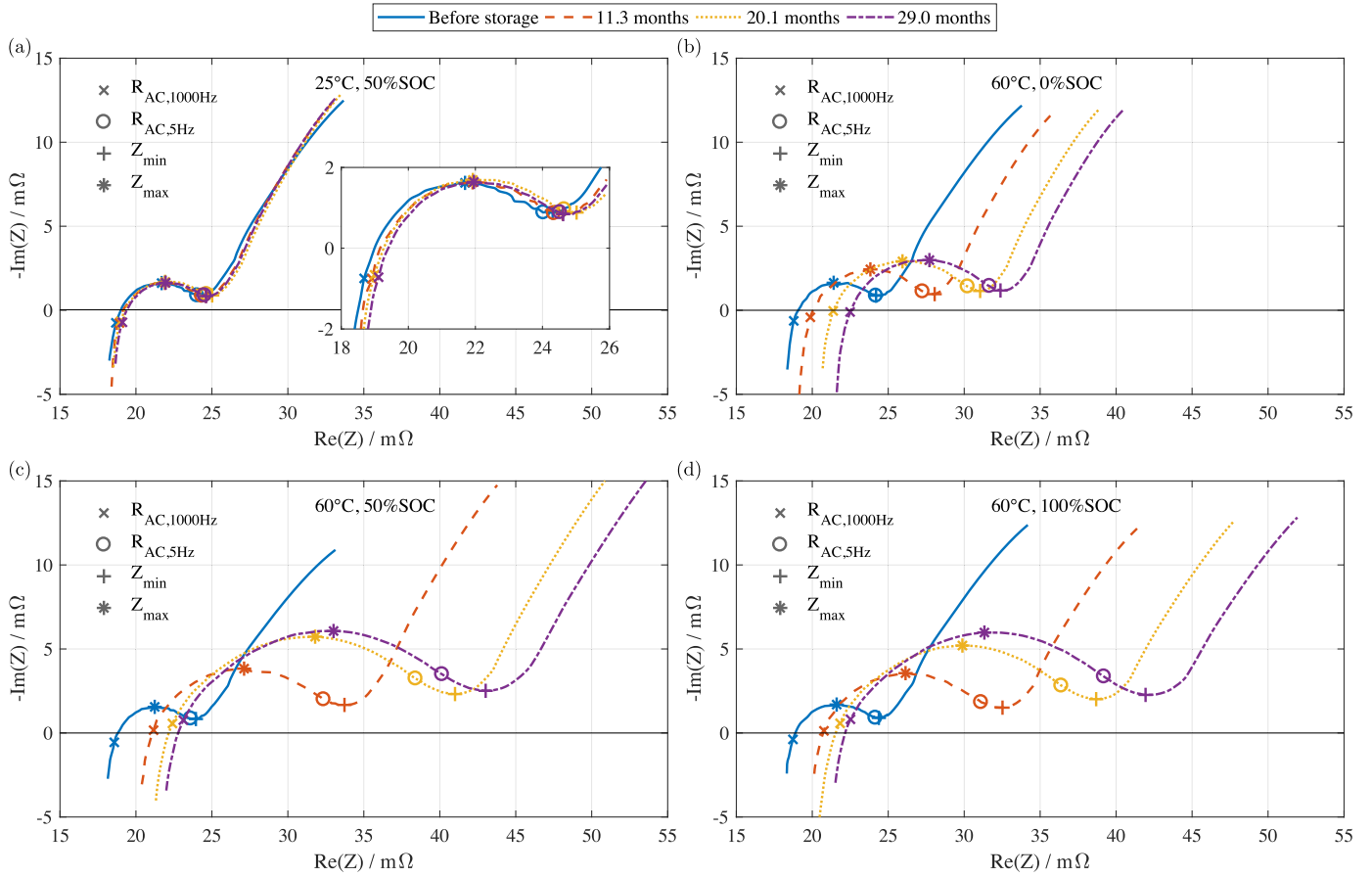| TP-Temp. -SOC Parameters	25 °C 50%	60 °C 0%	60 °C 50%	60 °C 100%
$R_{AC,1000Hz}$	2.3%	19.7%	24.5%	20.2%
$R_{AC,5Hz}$	2.0%	30.9%	70.1%	62.3%
Z_{min}	−1.9%	91.2%	292.2%	257.6%
$Re(Z_{min})$	−1.8%	92.5%	294.3%	259.9%
$Im(Z_{min})$	−4.3%	35.6%	201.7%	152.6%
Z_{max}	−3.5%	110.1%	313.0%	241.8%
$Re(Z_{max})$	−5.4%	122.5%	322.0%	237.4%
$Im(Z_{max})$	1.5%	85.5%	290.2%	253.2%

Fig. 5. EIS of selected TPs with different storage SOCs and temperatures at selected points in time during the aging study: (a) $SOC = 50\%$ at 25 °C. (b) $SOC = 0\%$ at 60 °C. (c) $SOC = 50\%$ at 60 °C. (d) $SOC = 100\%$ at 60 °C. The Nyquist-plots are drawn with an inverse *y*-axis due to the common form of presentation. In subplot (a) the area between 18 mΩ and 26 mΩ is displayed enlarged in an extra view in order to see more details. The parameters $R_{AC,1000\ Hz}$, $R_{AC,5\ Hz}$, Z_{min} and Z_{max} are displayed each with markers. The EIS measurement procedure is described in Section 2.3.

- $R_{AC,1000Hz}$ indicates the real part of the impedance measured with 1000 Hz, which is commonly applied for a quick characterization of the cell impedance.
- $R_{AC,5Hz}$ represents the real part of the impedance measured with 5 Hz and is used here to show the deviation of the impedance-curve due to the frequency.
- Z_{max} marks the local extremum of the impedance measured between 1000 Hz and 5 Hz.
- Z_{min} marks the local extremum of the impedance measured between Z_{max} and the impedances at the lowest frequencies on the right side.

The development of $R_{AC,1000Hz}$, $R_{AC,5Hz}$, Z_{max}, and Z_{min} together with the real and imaginary part of Z_{min} and Z_{max} are summarized in Table 6, where the relative change of each parameter from the beginning until the end of the aging study is shown for the selected TPs of Fig. 5.

The test point with a storage $SOC = 50\%$ at 25 °C shows only a slight shift of the EIS-curves to the right with higher resistances. However, the selected EIS-parameters that are shown in Table 6 increase very little for this test point. The decrease of Z_{min} and Z_{max} originate from the difficult exact determination of these parameters due to the flat curve shape in the respective areas. Little absolute measurement uncertainties lead to a big relative deviation of the extracted parameters' values.

The further TPs at 60 °C with $SOC = 0\%$, 50% and 100% show a stronger shift of the EIS-curves to the upper right during the aging study in Fig. 5b–d. Again a higher SOC leads to a stronger increase

of all impedances, however, at $SOC = 50\%$ the biggest increase of all impedances is observable. This behavior was also observed with the highest increase of $R_{DC,1Os}$ at $SOC = 50\%$ obtained in the CM shown in Fig. 2d. Table 6 shows these observations in more detail: For all SOCs at 60°C $R_{AC,1000Hz}$ increases by about 20%. However, the further EIS-parameters increase a lot more at $SOC = 50\%$ and 100% with the highest values at 50%.

3.2. Aging model development

In this subsection aging models are developed for both the relative discharge capacity C_{disch} and the relative resistance $R_{DC,1Os}$. For better comparability, in the following Q_{loss} represents the decrease/loss of the relative discharge capacity C_{disch} and R_{inc} the increase of the relative resistance $R_{DC,1Os}$. The aging model to be developed here should be able to represent the individual influence on the aging of the temperature T, SOC and passed time t since BOL. Furthermore, the model should be described with formulas that only depend on the influencing parameters (T, SOC and t) and a small set of constants that are determined separately for each influence parameter.

3.2.1. Model limitations

The measurement data shown in Section 3.1.1 revealed, that the capacity of the TPs with 0% SOC at 25 °C and 40 °C increased at the beginning of the aging study and decreased thereafter steadily. Furthermore, the resistance of most of the TPs decreased at the beginning of the aging study slightly and increased afterwards

Table 7
Q_{loss} and R_{inc} aging model reference values and parameters.

Parameter	Q_{loss}	R_{inc}
T_{ref}	298.15 K	298.15 K
SOC_{ref}	100%	100%
k_{ref}	0.0012571 %s^{-0.5}	3.4194×10^{-8} %s^{-1}
a	−2059.8	−8638.8
b	9.2644	29.992
E_a	17.126 kJ mol^{-1}	71.827 kJ mol^{-1}
c	2.8575	−3.3903
d	0.60225	1.5604

continuously. These inverse aging trends at the beginning of the test duration, which could be related to the effects of the anode overhang area, are not covered by the aging model. Due to the fact, that the aging model is developed for the application in BESS lifetime simulations, the fade of the useable capacity and the decrease of the performance in limited temperature and SOC ranges are required. Hence, the influence of the anode overhang effect is neglected, because BESS are normally not operated at very low or high SOC where this effects mainly occurs. Although the measured capacity values can deviate from the theoretical useable capacity maximal by about ±2.2% for the TPs with 0% and 100% SOC due to the effect of the anode overhang areas, the measured capacity values are used for the parametrization of the aging model without any adaption. Similarly, the measured resistance values are used with any adaption for the parametrization of the aging model.

3.2.2. Model structure

The development of Q_{loss} dependent on T, SOC and t is expressed by Eq. (3) and of R_{inc} with Eq. (4) in the form of a product that consists of three factors that represent the influence of T with $k_{temp,Q_{loss}/R_{inc}}(T)$, of SOC with $k_{soc,Q_{loss}/R_{inc}}(T)$ and of t individually. The formulas' factors are derived separately in the following and their parameters are shown in Table 7. There are different methods to determine the model parameters with the measurement data of this calendar aging study because the test matrix was designed redundantly. In the following we explain the different possibilities to obtain the model parameters, however, only the methods giving the best and most feasible results are applied in the aging model validation in Section 3.3.

$$Q_{loss}(T, (SOC), t)[\%] = \\ k_{temp,Q_{loss}}(T) \cdot k_{SOC,Q_{loss}}(SOC) \cdot \sqrt{t} \tag{3}$$

$$R_{inc}(T, SOC, t)[\%] = \\ k_{temp,R_{inc}}(T) \cdot k_{soc,R_{inc}}(SOC) \cdot t \tag{4}$$

3.2.3. Influence of time

Due to the fact that the rough trend of the capacity loss follows a square root dependance over time for most of TPs (see Fig. 2a and c), the time influence is therefore represented with the factor $\sqrt{t}$ for Q_{loss} in accordance with the models shown in different publications [25,35]. In contrast, the resistance increases rather linearly over time for most of TPs (see Fig. 2b and d). Consequently, the time influence is represented with the linear factor t for R_{inc}. However, the slight resistance increase for most of TPs at the beginning of the aging study cannot be represented with this aging model.

3.2.4. Influence of temperature

The temperature influence factor $k_{temp,Q_{loss}}(T)$ for Q_{loss} and $k_{temp,R_{inc}}(T)$ for R_{inc} can be modeled according to the Arrhenius-law, showing an exponential influence of the inverse of temperature on the resulting aging effect. Therefore the formula shown in Eq. (5),

which is commonly used to model the temperature influence on aging in different publications [39,30], is applied to determine $k_{temp,Q_{loss}}(T)$ for Q_{loss} and $k_{temp,R_{inc}}(T)$ for R_{inc} each with individual parameters but with the same formula structure. Due to the fact that the SOC influences the temperature non-linearly, all values have to be related to a reference temperature and SOC. Here the reference conditions are set with $T_{ref} = 25°C = 298.15$ K and $SOC_{ref} = 100\%$. In addition to the only influence parameter T, the formula consists of $R = 8.314$ J mol^{-1} K^{-1} representing the universal gas constant and two parameters representing the individual aging of the investigated cell: the reference aging rate $k_{ref,Q_{loss}/R_{inc}}$ and the activation energy $E_{a,Q_{loss}/R_{inc}}$, which are determined in the following for Q_{loss} and R_{inc} separately.

$$k_{temp,Q_{loss}/R_{inc}}(T) = \\ k_{ref,Q_{loss}/R_{inc}} \cdot \exp\left(-\frac{E_{a,Q_{loss}/R_{inc}}}{R}\left(\frac{1}{T} - \frac{1}{T_{ref}}\right)\right) \tag{5}$$

The reference aging rates $k_{ref,Q_{loss}}$ and $k_{ref,R_{inc}}$ can be obtained by transposing Eqs. (3) and (4) respectively, which leads to Eqs. (6) and (7). The factors representing the SOC influence $k_{SOC,Q_{loss}}(SOC)$ and $k_{SOC,R_{inc}}(SOC)$ can be set to a value of 1 because k_{ref} is defined with $SOC_{ref} = 100\%$. By using the reference temperature T_{ref} and therefore applying $T = 25°C$ in Eq. (5), the exponential term of Eq. (5) also obtains a value of 1. Thus $k_{ref,Q_{loss}}$ can be determined by dividing the measured value of Q_{loss} at the end of the aging study ($t = t_{end}$) from the TP with $T = 25 °C$ and $SOC = 100\%$ with the time factor $\sqrt{t_{end}}$. $k_{ref,R_{inc}}$ can be calculated similarly by dividing the measured value of R_{inc} at the end of the aging study ($t = t_{end}$) from the TP with $T = 25 °C$ and $SOC = 100\%$ with the time factor t_{end}.

$$k_{ref,Q_{loss}} = \frac{Q_{loss}(T_{ref} = 25 °C, SOC_{ref} = 100\%, t_{end})}{k_{SOC,Q_{loss}}(SOC_{ref} = 100\%) \cdot \sqrt{t_{end}}} \tag{6}$$

$$k_{ref,R_{inc}} = \frac{R_{inc}(T_{ref} = 25°C, SOC_{ref} = 100\%, t_{end})}{k_{SOC,R_{inc}}(SOC_{ref} = 100\%) \cdot t_{end}} \tag{7}$$

Although all parameters are thereby available to determine respectively $E_{a,Q_{loss}}$ and $E_{a,R_{inc}}$ in Eq. (5) by evaluating the aging of two TPs with the same SOC but different temperatures, $E_{a,Q_{loss}}$ and $E_{a,R_{inc}}$ are determined here with a fitting procedure to obtain better model results. Therefore, first Eq. (5) for $k_{temp,Q_{loss}}(T)$ and $k_{temp,R_{inc}}(T)$ are each inserted in Eqs. (3) and (4) respectively. Then the equations for Q_{loss} and R_{inc} can be expressed in a linear form by applying the natural logarithm on both sides, getting Eqs. (8) and (9) respectively.

$$\ln(Q_{loss}(T, SOC_{ref} = 100\%, t)) = \\ \underbrace{-\frac{E_{a,Q_{loss}}}{R}}_{a}\frac{1}{T} + \underbrace{\left(\frac{E_{a,Q_{loss}}}{R\,T_{ref}} + \ln(k_{ref,Q_{loss}} \cdot \sqrt{t})\right)}_{b} \tag{8}$$

$$\ln(R_{inc}(T, SOC_{ref} = 100\%, t)) = \\ \underbrace{-\frac{E_{a,R_{inc}}}{R}}_{a}\frac{1}{T} + \underbrace{\left(\frac{E_{a,R_{inc}}}{R\,T_{ref}} + \ln(k_{ref,R_{inc}} \cdot t)\right)}_{b} \tag{9}$$

Again $k_{SOC,Q_{loss}}(SOC)$ and $k_{SOC,R_{inc}}(SOC)$ can be set to a value of 1, because the equations are evaluated for $SOC_{ref} = 100\%$. Thus, we can derive linear formulas in the form $a \cdot \frac{1}{T} + b$. This linear relationship is shown in Fig. 6a and c respectively for Q_{loss} and R_{inc}, where Eqs. (8) and (9) are evaluated for selected points in time.

Here, only the temperatures 25 °C, 40 °C and 60 °C are shown and used for the fitting procedure. The aging of the TPs with 0 °C
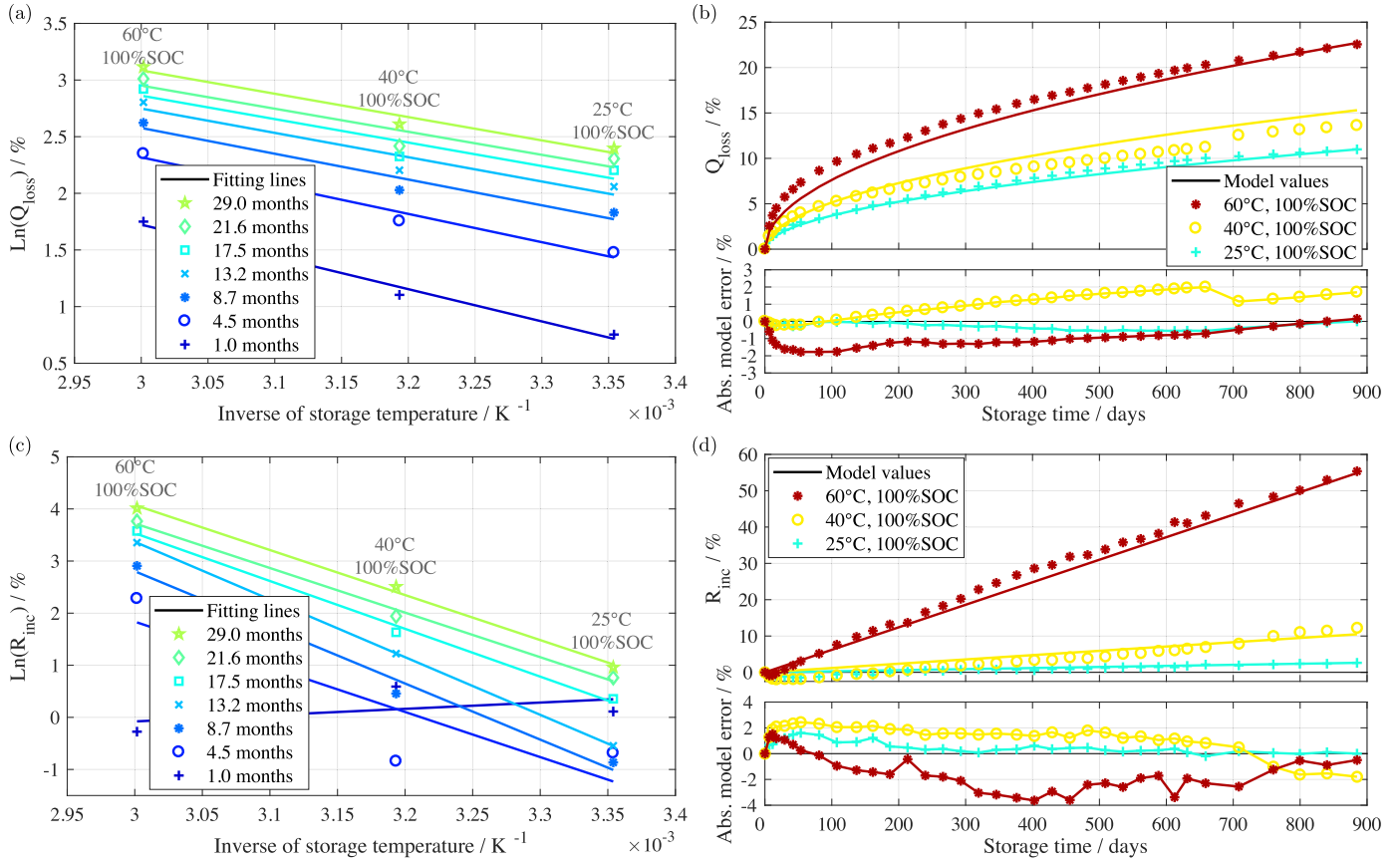
Fig. 6. Influence of temperature on aging of Q_{loss} and R_{inc} at $SOC = 100\%$ evaluated for the temperatures 25 °C, 40 °C and 60 °C: (a) Results of evaluating Q_{loss} with Eq. (8) and applying a linear fitting for each shown point in time. (c) Results of evaluating R_{inc} with Eq. (9) and applying a linear fitting for each shown point in time. (b)/(d) Comparison of measured values of Q_{loss}/R_{inc} with model values determined with Eq. (3)/Eq. (4). The lower panels show the absolute model error in %.

and 10 °C show ambiguous results and might, in comparison to the little calendar aging at the low temperatures, be strongly influenced by temperature deviations due to the periodic CM at 25 °C. For each point in time shown in Fig. 6, a linear fitting is applied resulting in lines with almost the same slope (factor a) at every point in time but shifted with an offset (factor b) dependent on the point in time. With this linear fitting in form of $a \cdot \frac{1}{T} + b$, $E_{a,Q_{loss}}$ and $E_{a,R_{inc}}$ can be obtained using the slope a at any time of the aging study (thus independent of b) with Eq. (10) for Q_{loss} and R_{inc} respectively.

$$E_{a,Q_{loss}/R_{inc}}(t_{end}) = -a_{Q_{loss}/R_{inc}}(t_{end}) \cdot R \qquad (10)$$

However, the model is parametrized by evaluating the slope at the end of the aging study ($t_{end} = 29$ months) leading to better model results. Having determined $E_{a,Q_{loss}/R_{inc}}$, the same fitting could be used to determine $k_{ref,Q_{loss}}$ and $k_{ref,R_{inc}}$ by transposing Eqs. (8) and (9) respectively. Nevertheless, better model results are obtained by determining $k_{ref,Q_{loss}}$ and $k_{ref,R_{inc}}$ by applying $T_{ref} = 25$ °C = 298.15 K in Eqs. (6) and (7) respectively. The results of the aging model with a static $SOC = 100\%$ for the temperatures 25 °C, 40 °C and 60 °C are compared with measured values in Fig. 6b for Q_{loss} and in Fig. 6d for R_{inc}. In Figs. 6b and d the lower panels show the absolute model errors in % for each TP for Q_{loss} and R_{inc} respectively. Q_{loss} can be estimated with this model for the TP at 25 °C and with $SOC = 100\%$ with almost no error. However, the model values deviate for the TPs with 40 °C and 60 °C up to 2% but follow the trend of the measured values well. The same observations apply for R_{inc}. However, the model values deviate for 60 °C up to 4% in the middle time segment of the aging study.

3.2.5. Influence of SOC

As shown in Fig. 2b and d, no linear trend is observable for the influence of SOC on calendar aging of Q_{loss} and R_{inc}. Furthermore, the aging trend neither follows the trend of the open circuit voltage (OCV)-values of each SOC nor the open-circuit voltages of each TP at the beginning of the CM. However, we develop empirical models for Q_{loss} and R_{inc} respectively, which should be able to follow the aging trend of a long time scale only influenced by the particular storage SOC-values.

Although a slight capacity increase is possible due to the effect of the anode overhang areas as mentioned above, this aging model is parametrized by the measured trend over time with static storage conditions. In order to model the step-like shape of Q_{loss} over SOC shown in Fig. 2b, a cubic function is applied to determine $k_{SOC,Q_{loss}}$ dependent on SOC with Eq. (12). The fitting is performed with the TPs at 40 °C leading to more pronounced differentiation with the 9 storage SOCs at this temperature. Then $k_{SOC,Q_{loss}}$ can be determined by transposing Eq. (3) resulting in Eq. (11). To obtain $k_{SOC,Q_{loss}}$ correctly, $k_{temp,Q_{loss}}(T)$ has to be adapted with $T = 40$ °C.

$$k_{SOC,Q_{loss}}(SOC) = \frac{Q_{loss}(T = 40°C, SOC, t)}{k_{temp,Q_{loss}}(T = 40°C) \cdot \sqrt{t}} \qquad (11)$$

$$k_{SOC,Q_{loss}}(SOC) = c_{Q_{loss}}(SOC - 0.5)^3 + d_{Q_{loss}} \qquad (12)$$

In Fig. 7a the results of Eq. (11) are drawn for selected points in time over the SOC of the TPs at 40 °C. The fitting lines are obtained by deriving a curve fit with Eq. (12) for each point in time including the whole SOC range. Even though the fitting lines of the first
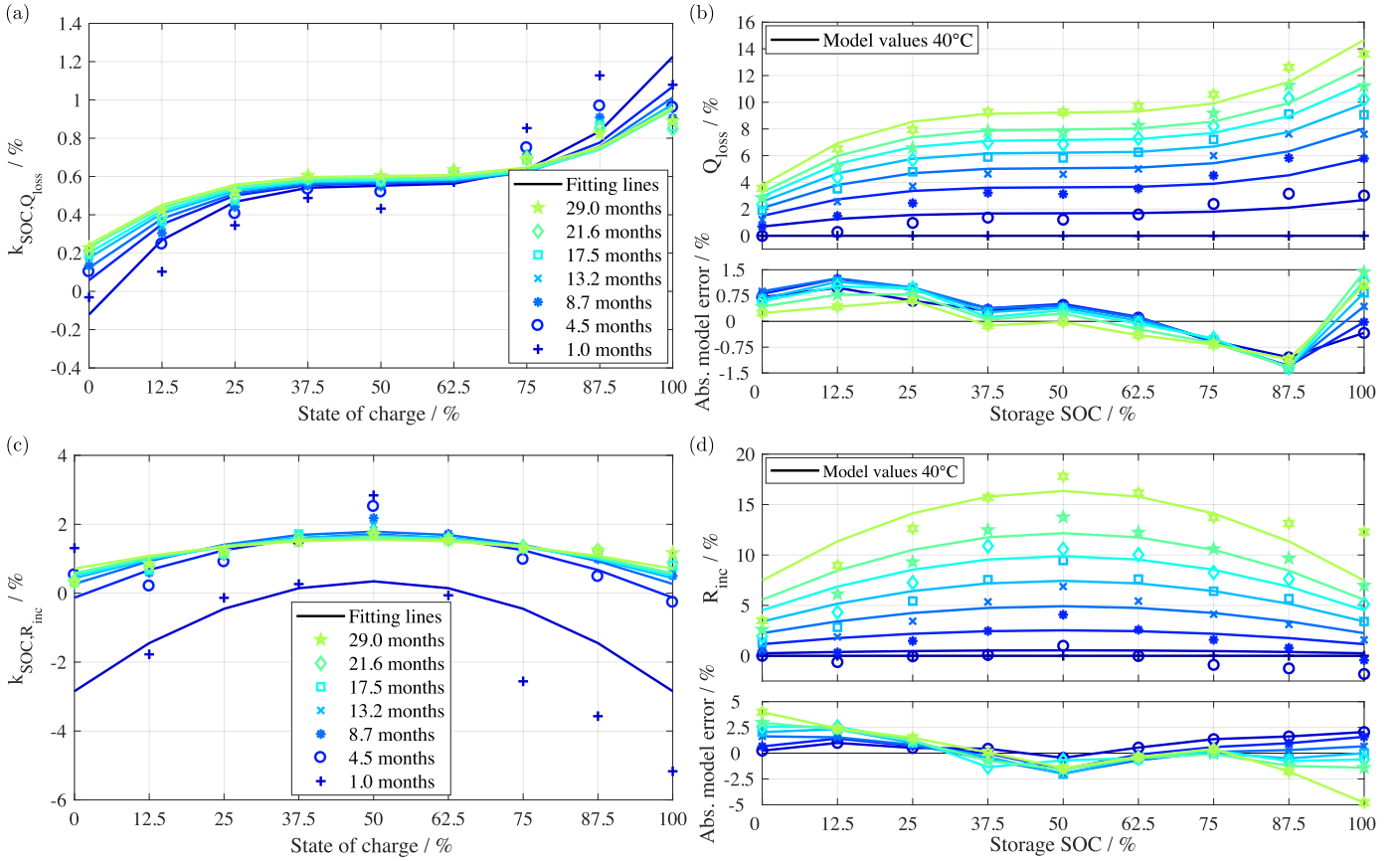
Fig. 7. Influence of SOC on aging of Q_{loss} and R_{inc} evaluated at 40 °C: (a) Results of evaluating Q_{loss} with Eq. (11) and applying a fitting with a cubic function for each shown point in time. (c) Results of evaluating R_{inc} with Eq. (13) and applying a fitting with a quadratic function for each shown point in time. (b)/(d) Comparison of measured values of Q_{loss}/ R_{inc} with model values determined with Eq. (3)/Eq. (4). The lower panels shows the absolute model error in %.

points in time deviate from the measured values, the fitting lines at the end of the aging study correspond well with the measurements. Therefore, the parameters $c_{Q_{loss}}$ and $d_{Q_{loss}}$ are obtained with a curve fit of $k_{SOC,Q_{loss}}$ at the end of aging study ($t_{end} = 29$ months), resulting in the parameter values shown in Table 7 for Q_{loss}. Fig. 7b shows the model values calculated with Eq. (3) by applying the here determined $k_{SOC,Q_{loss}}$ factor in comparison with the measured values of the TPs at 40 °C. The lower panel again shows the absolute model error in %, which stays below 1.5% over the whole SOC range during the entire aging study. However, the resulting capacity losses at the TPs with $SOC = 87.5\%$ and 100% show larger errors compared to the lower SOCs.

In order to model the triangular shape of R_{inc} over SOC shown in Fig. 2d, a quadratic function is applied to determine $k_{SOC,R_{inc}}$ dependent on SOC with Eq. (14). Similar to the procedure to determine $k_{SOC,Q_{loss}}$, the fitting for $k_{SOC,R_{inc}}$ is executed with the TPs at 40 °C. Again $k_{SOC,R_{inc}}$ can be determined by transposing Eq. (4) resulting in Eq. (13) and using $k_{temp,R_{inc}}(T)$ with $T = 40$ °C.

$$k_{SOC,R_{inc}}(SOC) = \frac{R_{inc}(T = 40\,°C, SOC, t)}{k_{temp,R_{inc}}(T = 40\,°C) \cdot t} \tag{13}$$

$$k_{SOC,R_{inc}}(SOC) = c_{R_{inc}}(SOC - 0.5)^2 + d_{R_{inc}} \tag{14}$$

In Fig. 7c the results of Eq. (13) are drawn for selected points in time over the SOC of the TPs at 40 °C. The fitting lines are obtained by deriving a curve fit with Eq. (14) for each point in time including the whole SOC-range. Again the fitting lines of the first points in time deviate from the measured values, however, the fitting lines

at the end of the aging study match well the measured values. Thus, the parameters $c_{R_{inc}}$ and $d_{R_{inc}}$ are obtained with a curve fit of $k_{SOC,R_{inc}}$ at the end of aging study ($t_{end} = 29$ months), resulting in the parameter values shown in Table 7 for R_{inc}. Fig. 7d shows the model values calculated with Eq. (4) by applying the here determined $k_{SOC,R_{inc}}$ factor in comparison with the measured values of the TPs at 40 °C. The lower panel again shows the absolute model error in %, which stays below 2.5% for most of the SOC values during the entire aging study. However, larger model errors result at $SOC = 0\%$ and 100%.

3.3. Aging model validation

Subsequent to the aging model development which proved a good consistency for static conditions, here the performance of the aging model for dynamic storage conditions is evaluated with the measurements from the dynamic calendar aging study (see Section 2.6). To apply the model equations with variable temperatures or SOCs over time, a differential form of the aging models is derived by differentiating Eq. (3) with respect to time for Q_{loss} getting Eq. (15) and differentiating Eq. (4) for R_{inc} resulting in Eq. (16).

$$\frac{dQ_{loss}}{dt}(T, SOC, t)[\%s^{-1}] = q_{loss}(T, SOC, t) = \\ k_{temp,Q_{loss}}(T) \cdot k_{soc,Q_{loss}}(SOC) \cdot (2\sqrt{t})^{-1} \tag{15}$$

$$\frac{dR_{inc}}{dt}(T, SOC)[\%s^{-1}] = r_{inc}(T, SOC) = \\ k_{temp,R_{inc}}(T) \cdot k_{soc,R_{inc}}(SOC) \tag{16}$$
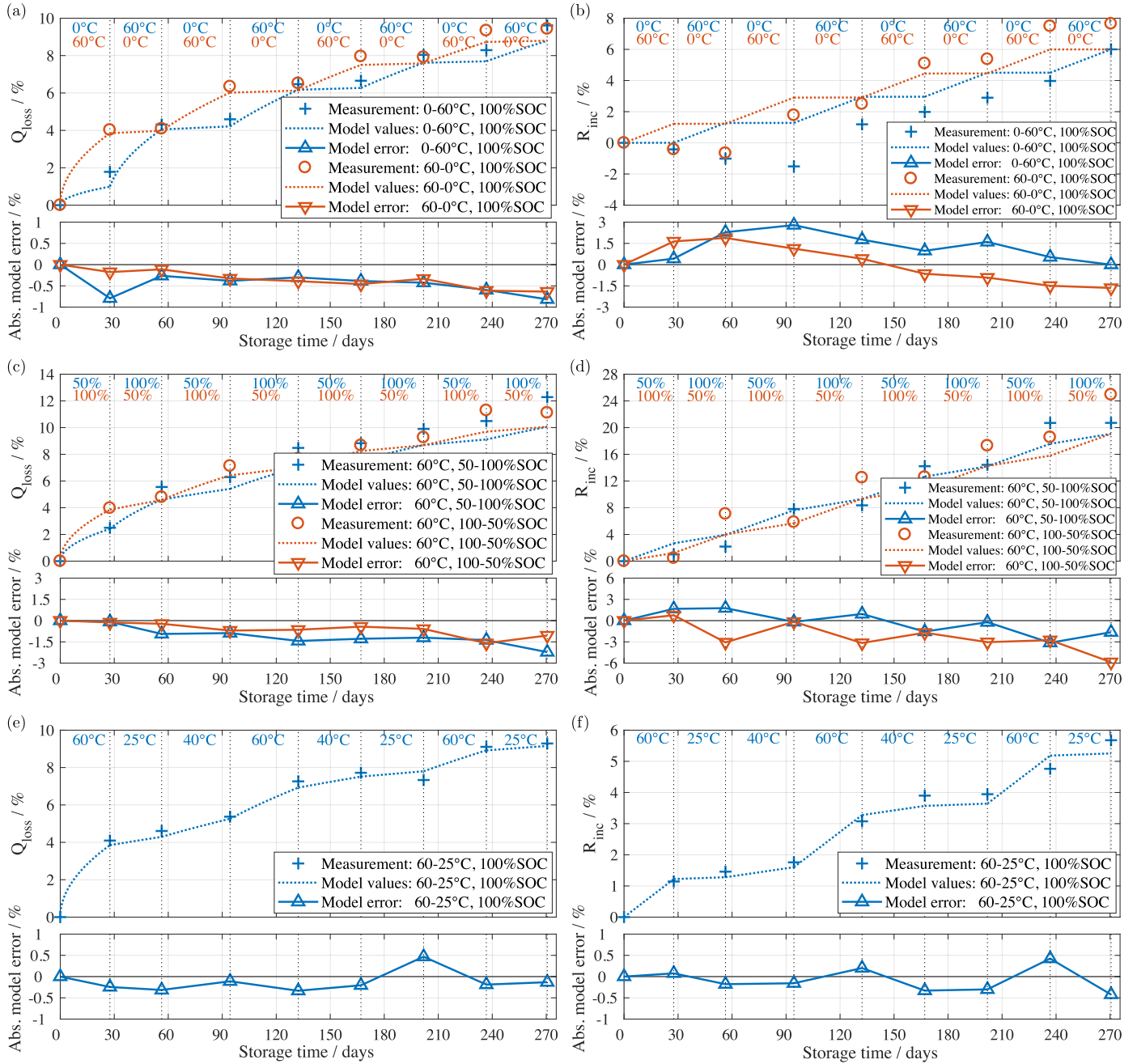
Fig. 8. Aging model validation with dynamic calendar aging study over 270 days with 8 intervals each with constant storage conditions. Each measurement represents one cell whose storage condition, temperature or SOC, is changed after one interval according to the test matrix Table 5. In every plot the lower panel shows the absolute model error in % compared to the measured values. The plots on the left side represent the capacity loss and the plots on the right side resistance increase of each TP. (a/b) TP7/TP8 with switching between storage temperature 0 °C and 60 °C at storage SOC = 100%. TP7 (blue) starts with 0 °C and TP8 (red) with 60 °C. (c/d) TP13/TP14 with switching between storage SOC = 50% and 100% at storage temperature 60 °C. TP1 (blue) starts with SOC = 50% and TP14 (red) with SOC = 100%. (e/f) TP15 with changing storage temperature dynamically between 60 °C, 25 °C and 40 °C at storage SOC = 100%. (For interpretation of the references to color in this figure legend, the reader is referred to the web version of the article.)

Furthermore, it has to be identified how to apply the aging models correctly when the storage conditions are varied. The results of the dynamic calendar aging study show (see Fig. 8) the independence of the order of storage conditions. Additionally it can be concluded that the calendar aging rate is dependent on the current SOH. Thus the particular SEI growth depends on former aging history (SEI thickness). Hence, to determine the differential capacity loss q_{loss} when varying the storage conditions, the virtual time t^* is defined, representing the time until the same Q_{loss} is reached under the new storage conditions. As the resistance increase is constant over time, no additional measures for time

compensation of R_{inc} have to be taken. The virtual time t^* can be derived by solving Eq. (3) for time resulting in Eq. (17) for Q_{loss}.

$$t_{Q_{loss}}^{*cal}(T, SOC, Q_{loss}) = \left(\frac{Q_{loss}}{k_{temp,Q_{loss}}(T) \cdot k_{soc,Q_{loss}}(SOC)} \right)^2 \quad (17)$$

Thus, when applying the aging model with changing storage conditions, the virtual time t^* has to be determined for each time step. Then t^* is applied to calculate the differential capacity loss q_{loss} in the next time interval with new storage conditions.

Table 8
Absolute model errors of Q_{loss} and R_{inc} of all TPs of the dynamic calendar aging study.

Test point	Temperature	SOC	Absolute model error at EOT	
			Q_{loss}	R_{inc}
TP1/TP2	25/40 °C	100%	+1.1%/+1.2%	+1.6%/+1.6%
TP3/TP4	25/60 °C	100%	+0.0%/−0.3%	−1.5% / −0.8%
TP5/TP6	40/60 °C	100%	−0.1% / −0.1%	−0.7% / −2.4%
TP7/TP8	0/60 °C	100%	−0.8% / −0.6%	+0.0% / −1.6%
TP9/TP10	60 °C	0/50%	−1.9% / +0.5%	−4.7% / +6.9%
TP11/TP12	60 °C	0/100%	−2.2% / −1.9%	−2.9% / +0.0%
TP13/TP14	60 °C	50/100%	−2.2% / −1.1%	−1.6% / −5.9%
TP15	Dynamic	100%	−0.1%	−0.4%

Based on these equations for the application of the aging models of Q_{loss} and R_{inc}, the results of the dynamic calendar aging study can be compared with the developed aging model. For selected TPs (see Table 5) Fig. 8 shows the measured aging results in comparison with the model values for Q_{loss} on the left side with Fig. 8a, c and e and for R_{inc} on the right side with Fig. 8b, d and f. In every plot the lower panel shows the absolute model error in % compared to the measured values. The storage conditions of each TP are switched 7 times each at time intervals of about 4 weeks. The results of all TPs of this dynamic calendar aging study are summarized in Table 8 alongside with the absolute model error of Q_{loss} and R_{inc} at the end of the test.

Fig. 8a/b represent the TP7/TP8 with switching between the storage temperatures 0 °C and 60 °C at storage $SOC = 100\%$ with two cells. TP7 (blue) starts with 0 °C and TP8 (red) with 60 °C. Here, always after two time intervals, the two cells reach almost the same Q_{loss} value, proving the theory of independence of the order of storage conditions. The model values for each cell very closely follow the measured values even when the storage temperature changes. The error increases slightly over time but underestimates Q_{loss} by less than 1%. For R_{inc} the observations are different since the resistances decreased in this TP at the beginning. Afterwards, the R_{inc} values of the two cells get closer again but do not match each other as well as the Q_{loss} values. Even though the model cannot represent the R_{inc} in the beginning, the subsequent increase is estimated with errors below 1.5%.

Fig. 8c/d show the TP13/TP14 with alternating between the storage $SOC = 50\%$ and 100% at 60 °C with two cells. TP13 (blue) starts with $SOC = 50\%$ and TP14 (red) with $SOC = 100\%$. Again the two cells' Q_{loss} values each meet after two passed time intervals, but not as close as observed with in TP4. The model values follow the measured values but underestimate the measured values by around 1.5% at the end of the aging study. In contrast to the TP7/TP8, here the R_{inc} values remain close together over all intervals. Although the model values show an error of about 6% for cell 2 at the end of the aging study, the model follows the trend of the measured values.

Fig. 8e/f illustrate the TP15 with changing storage temperature dynamically between 60 °C, 25 °C and 40 °C at storage $SOC = 100\%$ with one cell. Here, the model follows the measured Q_{loss} values very well and the model error is not increasing over time by remaining below 0.5%. The same applies for R_{inc}, although the increase rates are changing stronger than seen for Q_{loss}.

4. Conclusions

This static calendar aging study on commercial LFP/C cells with 17 TPs with 3 cells each over almost 900 days reveals a strong influence of storage temperature and SOC on both capacity loss and resistance increase. In line with literature, the observed calendar aging of LFP/C cells leads predominantly to LLI due to the SEI growth on the graphite anode and only minor contributions from LAM. Hence, Q_{loss} and R_{inc} are increasing over time, however, the rate of Q_{loss} is slowing down in a square root dependance over time. In contrast, the rate of R_{inc} stays constant over time. The temperature influence appeared as observed in other aging studies, showing an exponential dependency of the increase rate of Q_{loss} and R_{inc} with respect to the storage temperature. The influence of storage SOC on Q_{loss} over time showed similar results as observed in [14]. With higher storage SOCs the rates of Q_{loss} are increasing, but in the middle SOC-range, the rate stays almost constant. In contrast, R_{inc} showed the highest values in the middle SOC-range.

Based on the static calendar aging study, a semi-empirical model was developed to estimate Q_{loss} and R_{inc} for the influence of temperature, SOC and time. The resulting aging equations are products that consist of three factors, each representing one of the influence parameters. The temperature influence can be modeled with the widely used Arrhenius-term for both Q_{loss} and R_{inc}. However, due to the long test duration, this study proves that the temperature influence can be modeled with the Arrhenius-term over long time scales. The temperature factor parameters have been determined with the TPs at $SOC = 100\%$ of 25 °C, 40 °C and 60 °C. The SOC influence factor was modeled with a cubic function for Q_{loss} and a quadratic function for R_{inc}. The functions' parameters have been determined with the TPs at 40 °C with 9 SOC values between 0 and 100%.

The necessary equations for the rate of Q_{loss} and R_{inc} have been derived for the application of the aging model in lifetime simulations. Furthermore, an equation for the virtual time t^* was introduced which enables the correct simulation of varying storage conditions when applying the aging model.

Finally, the aging model was validated with the measurement values of a dynamic calendar aging study. This study proved the hypothesis of independence of the order of storage conditions on the resulting Q_{loss} and R_{inc} and the fact that the calendar aging rate is dependent on the current SOH. The aging model is able to estimate the aging of the dynamic calendar aging TPs fairly accurately with a maximum absolute error of 2.2% for Q_{loss} and 6.9% for R_{inc}. This paper shows that the aging of the investigated LFP/C cells can be estimated relatively precisely with a semi-empirical aging model based on few fitting parameters that do not have to be adapted for each storage condition. Due to the good correspondence of the temperature influence on Q_{loss} and R_{inc} with the Arrhenius-law, an extrapolation passing the measurement time of almost 900 days is allowed leading to calendar lifetime of more than 22 years (assuming a EOL at $Q_{loss} = 20\%$) for the storage conditions with 25 °C at $SOC = 50\%$. Assuming a operating life of 20 years for stationary battery systems [1,5], the calendar aging of the investigated LFP/C cell would account for about 19.0% decrease of the initial capacity and about 33.7% increase of the initial resistance in case that the SOC remains at 50% and the temperature at 25 °C. By considering the additional cycle aging of a stationary battery application, the capacity would underrun the EOL criteria at typically $Q_{loss} = 20\%$ before having passed 20 years of operating life with the described operation conditions.

In order to reduce the measurement efforts in future calendar aging studies on LFP/C cells, the test matrix could cover only two temperatures: one with the standard conditions of application (e.g. 25 °C) and the second at the highest possible operation temperature (e.g. 60 °C).

Because the SOC-influence on calendar aging of Q_{loss} and R_{inc} does not follow the storage SOC in a simple functional dependance, the TPs should cover various SOC values (e.g. with multiple points of support, evenly spaced or aggregated at the SOC-values where phase changes of the graphite anode are expected).

5. Outlook

In order to estimate the calendar and the cycle aging of BESS operation with LFP/C cells, an aging model is needed covering both aging mechanisms. Consequently, a cycle aging study on the here investigated LFP/C cell covering most of the possible influence parameters on aging was performed simultaneously to this study and is going to be published. Pure cycle aging can be derived using the results of this calendar aging model. Then both aging mechanisms can be integrated into a comprehensive aging model covering both calendar and cycle aging. Furthermore, this complete aging is going to be validated with dynamic profiles of different BESS application scenarios within a future publication. This complete aging model can then be used, for example, in techno-economic simulation of stationary BESS in order to assess the impact of battery aging. Thereby the component sizing and the control algorithms of BESS operation can be optimized with respect to estimated battery aging. Even though the aging model presented here is able to estimate the influence of SOC on capacity loss and resistance increase with an empirical approach accurately, the SOC dependance should be analyzed and explained with physico-chemical models more thorough in future studies. Furthermore, in order to model influence of the anode overhang effect on the useable cell capacity and resistance properly, further measurements and possibly post-mortem analysis of the investigated cell are necessary in future investigations.

Acknowledgements

References

[1] M. Naumann, R.C. Karl, C.N. Truong, A. Jossen, H.C. Hesse, Lithium-ion battery cost analysis in pv-household application, Energy Procedia 73 (2015) 37–47, doi:http://dx.doi.org/10.1016/j.egypro.2015.07.555.

[2] M. Yasuda, Sony energy storage system using olivine type battery, International Conference on Olivines for Rechargeable Batteries, Montreal, 2014.

[3] Kokam Battery Cells, Lithium ion polymer cells - high energy high power (22.12.17). http://kokam.com/cell/.

[4] F. Gatta, A. Geri, R. Lamedica, S. Lauria, M. Maccioni, F. Palone, M. Rebolini, A. Ruvio, Application of a LiFePO4 battery energy storage system to primary frequency control: simulations and experimental results, Energies 9 (12) (2016) 887, doi:http://dx.doi.org/10.3390/en9110887.

[5] A. Zeh, M. Müller, M. Naumann, H. Hesse, A. Jossen, R. Witzmann, Fundamentals of using battery energy storage systems to provide primary control reserves in Germany, Batteries 2 (3) (2016) 29, doi:http://dx.doi.org/10.3390/batteries2030029.

[6] J. Schmalstieg, S. Käbitz, M. Ecker, D.U. Sauer, A holistic aging model for li (nimnco)o2 based 18650 lithium-ion batteries, J. Power Sources 257 (2014) 325–334, doi:http://dx.doi.org/10.1016/j.jpowsour.2014.02.012.

[7] Technical University of Munich, Web portal of the energy neighbor (22.12.17). https://www.energyneighbor.de/en/home.html.

[8] C.N. Truong, M. Schimpe, M. Naumann, A. Jossen, H.C. Hesse, Impact of sub-components on the overall performance of stationary battery systems: insights on the prototype energy neighbor, International ETG Congress 2017, Bonn, Germany, 2017, pp. 1–6 URL: http://ieeexplore.ieee.org/stamp/stamp.jsp?tp=&arnumber=8278767&isnumber=8278714.

[9] Technical University of Munich, Eebatt – interdisciplinary energy storage research project. (22.12.17). https://www.mse.tum.de/en/eebatt/.

[10] M. Lepiorz, Betriebsbedingte Alterung von Lithium-Ionen Batterien in stationären und mobilen Anwendungen, dissertation, 1st ed., Ingenieurswissenschaften, Verlag Dr. Hut, Munich, 2016.

[11] A. Barré, B. Deguilhem, S. Grolleau, M. Gérard, F. Suard, D. Riu, A review on lithium-ion battery ageing mechanisms and estimations for automotive applications, J. Power Sources 241 (2013) 680–689, doi:http://dx.doi.org/10.1016/j.jpowsour.2013.05.040.

[12] D. Li, D.L. Danilov, L. Gao, Y. Yang, P.H.L. Notten, Degradation mechanisms of the graphite electrode in C6/LiFePO4 batteries unraveled by a non-destructive approach, J. Electrochem. Soc. 163 (14) (2016) A3016–A3021, doi:http://dx.doi.org/10.1149/2.0821614jes.

[13] D. Li, D.L. Danilov, J. Xie, L. Raijmakers, L. Gao, Y. Yang, P.H. Notten, Degradation mechanisms of C6/LiFePO4 batteries: experimental analysis of calendar aging, Electrochim. Acta 190 (2016) 1124–1133, doi:http://dx.doi.org/10.1016/j.electacta.2015.12.161.

[14] P. Keil, S.F. Schuster, J. Wilhelm, J. Travi, A. Hauser, R.C. Karl, A. Jossen, Calendar aging of lithium-ion batteries, J. Electrochem. Soc. 163 (9) (2016) A1872–A1880, doi:http://dx.doi.org/10.1149/2.0411609jes.

[15] B. Gyenes, D.A. Stevens, V.L. Chevrier, J.R. Dahn, Understanding anomalous behavior in coulombic efficiency measurements on li-ion batteries, J. Electrochem. Soc. 162 (3) (2014) A278–A283, doi:http://dx.doi.org/10.1149/2.0191503jes.

[16] M. Lewerenz, J. Münnix, J. Schmalstieg, S. Käbitz, M. Knips, D.U. Sauer, Systematic aging of commercial LiFePO4-graphite cylindrical cells including a theory explaining rise of capacity during aging, J. Power Sources 345 (2017) 254–263, doi:http://dx.doi.org/10.1016/j.jpowsour.2017.01.133.

[17] M. Lewerenz, A. Warnecke, D.U. Sauer, Post-mortem analysis on LiFePO4-graphite cells describing the evolution & composition of covering layer on anode and their impact on cell performance, J. Power Sources 369 (2017) 122–132, doi:http://dx.doi.org/10.1016/j.jpowsour.2017.10.003.

[18] J. Wilhelm, S. Seidlmayer, P. Keil, J. Schuster, A. Kriele, R. Gilles, A. Jossen, Cycling capacity recovery effect: a coulombic efficiency and post-mortem study, J. Power Sources 365 (2017) 327–338, doi:http://dx.doi.org/10.1016/j.jpowsour.2017.08.090.

[19] A. Eddahech, O. Briat, J.-M. Vinassa, Performance comparison of four lithium-ion battery technologies under calendar aging, Energy 84 (2015) 542–550, doi:http://dx.doi.org/10.1016/j.energy.2015.03.019.

[20] M. Kassem, J. Bernard, R. Revel, S. Pélissier, F. Duclaud, C. Delacourt, Calendar aging of a graphite/LiFePO4 cell, J. Power Sources 208 (2012) 296–305, doi:http://dx.doi.org/10.1016/j.jpowsour.2012.02.068.

[21] Y. Zheng, Y.-B. He, K. Qian, B. Li, X. Wang, J. Li, C. Miao, F. Kang, Effects of state of charge on the degradation of LiFePO4/graphite batteries during accelerated storage test, J. Alloys Comp. 639 (2015) 406–414, doi:http://dx.doi.org/10.1016/j.jallcom.2015.03.169.

[22] I. Bloom, B. Cole, J. Sohn, S. Jones, E. Polzin, V. Battaglia, G. Henriksen, C. Motloch, R. Richardson, T. Unkelhaeuser, D. Ingersoll, H. Case, An accelerated calendar and cycle life study of li-ion cells, J. Power Sources 101 (2) (2001) 238–247, doi:http://dx.doi.org/10.1016/S0378-7753(01)00783-2.

[23] M. Ecker, N. Nieto, S. Käbitz, J. Schmalstieg, H. Blanke, A. Warnecke, D.U. Sauer, Calendar and cycle life study of li(nimnco)o2-based 18650 lithium-ion batteries, J. Power Sources 248 (2014) 839–851, doi:http://dx.doi.org/10.1016/j.jpowsour.2013.09.143.

[24] P. Keil, A. Jossen, Calendar aging of NCA lithium-ion batteries investigated by differential voltage analysis and coulomb tracking, J. Electrochem. Soc. 164 (1) (2017) A6066–A6074, doi:http://dx.doi.org/10.1149/2.0091701es.

[25] E. Sarasketa-Zabala, I. Gandiaga, L.M. Rodriguez-Martinez, I. Villarreal, Calendar ageing analysis of a LiFePO4/graphite cell with dynamic model validations: towards realistic lifetime predictions, J. Power Sources 272 (2014) 45–57, doi:http://dx.doi.org/10.1016/j.jpowsour.2014.08.051.

[26] M. Swierczynski, D.-I. Stroe, A.-I. Stan, R. Teodorescu, S.K. Kaer, Lifetime estimation of the nanophosphate LiFePO4/c battery chemistry used in fully electric vehicles, IEEE Trans. Ind. Appl. 51 (4) (2015) 3453–3461, doi:http://dx.doi.org/10.1109/TIA.2015.2405500.

[27] E.V. Thomas, I. Bloom, J.P. Christophersen, V.S. Battaglia, Rate-based degradation modeling of lithium-ion cells, J. Power Sources 206 (2012) 378–382, doi:http://dx.doi.org/10.1016/j.jpowsour.2012.01.106.

[28] S. Käbitz, J.B. Gerschler, M. Ecker, Y. Yurdagel, B. Emmermacher, D. Andr, T. Mitsch, D.U. Sauer, Cycle and calendar life study of a graphite-LiNi1/3Mn1/3Co1/3O2 li-ion high energy system. Part a: full cell characterization, J. Power Sources 239 (2013) 572–583, doi:http://dx.doi.org/10.1016/j.jpowsour.2013.03.045.

[29] L. Su, J. Zhang, J. Huang, H. Ge, Z. Li, F. Xie, B.Y. Liaw, Path dependence of lithium ion cells aging under storage conditions, J. Power Sources 315 (2016) 35–46, doi:http://dx.doi.org/10.1016/j.jpowsour.2016.03.043.

[30] S. Grolleau, A. Delaille, H. Gualous, P. Gyan, R. Revel, J. Bernard, E. Redondo-Iglesias, J. Peter, Calendar aging of commercial graphite/LiFePO4 cell – predicting capacity fade under time dependent storage conditions, J. Power Sources 255 (2014) 450–458, doi:http://dx.doi.org/10.1016/j.jpowsour.2013.11.098.

[31] M. Petit, E. Prada, V. Sauvant-Moynot, Development of an empirical aging model for li-ion batteries and application to assess the impact of vehicle-to-grid strategies on battery lifetime, Appl. Energy 172 (2016) 398–407, doi:http://dx.doi.org/10.1016/j.apenergy.2016.03.119.

[32] M. Broussely, S. Herreyre, P. Biensan, P. Kasztejna, K. Nechev, R. Staniewicz, Aging mechanism in li ion cells and calendar life predictions, J. Power Sources 97–98 (2001) 13–21, doi:http://dx.doi.org/10.1016/S0378-7753(01)00722-4.

[33] M. Ecker, J.B. Gerschler, J. Vogel, S. Käbitz, F. Hust, P. Dechent, D.U. Sauer, Development of a lifetime prediction model for lithium-ion batteries based on extended accelerated aging test data, J. Power Sources 215 (2012) 248–257, doi:http://dx.doi.org/10.1016/j.jpowsour.2012.05.012.

[34] K. Smith, E. Wood, S. Santhanagopalan, G.-H. Kim, J. Neubauer, A. Pesaran, Models for battery reliability and lifetime, Battery Congress 2013 (2013) 1–8.

[35] J. Wang, J. Purewal, P. Liu, J. Hicks-Garner, S. Soukazian, E. Sherman, A. Sorenson, L. Vu, H. Tataria, M.W. Verbrugge, Degradation of lithium ion batteries employing graphite negatives and nickel-cobalt-manganese oxide + spinel manganese oxide positives: Part 1 aging mechanisms and life estimation, J. Power Sources 269 (2014) 937–948, doi:http://dx.doi.org/10.1016/j.jpowsour.2014.07.030.

[36] C. Delacourt, M. Safari, Life simulation of a graphite/LiFePO$_4$ cell under cycling and storage, J. Electrochem. Soc. 159 (8) (2012) A1283–A1291, doi:http://dx.doi.org/10.1149/2.049208jes.

[37] H. Ekström, G. Lindbergh, A model for predicting capacity fade due to SEI formation in a commercial graphite/LiFePO$_4$ cell, J. Electrochem. Soc. 162 (6) (2015) A1003–A1007, doi:http://dx.doi.org/10.1149/2.0641506jes.

[38] M. Safari, C. Delacourt, Simulation-based analysis of aging phenomena in a commercial graphite/LiFePO$_4$ cell, J. Electrochem. Soc. 158 (12) (2011) A1436, doi:http://dx.doi.org/10.1149/2.103112jes.

[39] E. Prada, D. Di Domenico, Y. Creff, J. Bernard, V. Sauvant-Moynot, F. Huet, A simplified electrochemical and thermal aging model of LiFePO$_4$-graphite li-ion batteries: power and capacity fade simulations, J. Electrochem. Soc. 160 (4) (2013) A616–A628, doi:http://dx.doi.org/10.1149/2.053304jes.

[40] K.L. Gering, Novel method for evaluation and prediction of capacity loss metrics in li-ion electrochemical cells, Electrochim. Acta 228 (2017) 636–651, doi:http://dx.doi.org/10.1016/j.electacta.2017.01.052.

[41] M. Lewerenz, S. Käbitz, M. Knips, J. Münnix, J. Schmalstieg, A. Warnecke, D.U. Sauer, New method evaluating currents keeping the voltage constant for fast and highly resolved measurement of arrhenius relation and capacity fade, J. Power Sources 353 (2017) 144–151, doi:http://dx.doi.org/10.1016/j.jpowsour.2017.03.136.

[42] K.L. Gering, S.V. Sazhin, D.K. Jamison, C.J. Michelbacher, B.Y. Liaw, M. Dubarry, M. Cugnet, Investigation of path dependence in commercial lithium-ion cells chosen for plug-in hybrid vehicle duty cycle protocols, J. Power Sources 196 (7) (2011) 3395–3403, doi:http://dx.doi.org/10.1016/j.jpowsour.2010.05.058.

[43] Z. Ma, J. Jiang, W. Shi, W. Zhang, C.C. Mi, Investigation of path dependence in commercial lithium-ion cells for pure electric bus applications: aging mechanism identification, J. Power Sources 274 (2015) 29–40, doi:http://dx.doi.org/10.1016/j.jpowsour.2014.10.006.

[44] M. Lepiorz, W. Weydanz, A. Jossen, Ah-throughput versus residual capacity method for prediction of capacity loss of li-ion batteries at alternating temperatures, Kraftwerk Batterie, Haus der Technik e.V. (2013).

[45] K. Rumpf, M. Naumann, A. Jossen, Experimental investigation of parametric cell-to-cell variation and correlation based on 1100 commercial lithium-ion cells, J. Energy Storage 14 (2017) 224–243, doi:http://dx.doi.org/10.1016/j.est.2017.09.010.

[46] M. Schimpe, M. Naumann, N. Truong, H.C. Hesse, S. Santhanagopalan, A. Saxon, A. Jossen, Energy efficiency evaluation of a stationary lithium-ion battery container storage system via electro-thermal modeling and detailed component analysis, Appl. Energy 210 (2018) 211–229, doi:http://dx.doi.org/10.1016/j.apenergy.2017.10.129.

[47] Y. Zheng, M. Ouyang, L. Lu, J. Li, Understanding aging mechanisms in lithium-ion battery packs: from cell capacity loss to pack capacity evolution, J. Power Sources 278 (2015) 287–295, doi:http://dx.doi.org/10.1016/j.jpowsour.2014.12.105.

[48] M. Lewerenz, A. Warnecke, D.U. Sauer, Introduction of capacity difference analysis (cda) for analyzing lateral lithium-ion flow to determine the state of covering layer evolution, J. Power Sources 354 (2017) 157–166, doi:http://dx.doi.org/10.1016/j.jpowsour.2017.04.043.

[49] F.M. Kindermann, A. Noel, S.V. Erhard, A. Jossen, Long-term equalization effects in li-ion batteries due to local state of charge inhomogeneities and their impact on impedance measurements, Electrochim. Acta 185 (2015) 107–116, doi:http://dx.doi.org/10.1016/j.electacta.2015.10.108.

[50] A.J. Smith, J.C. Burns, D. Xiong, J.R. Dahn, Interpreting high precision coulometry results on li-ion cells, J. Electrochem. Soc. 158 (10) (2011) A1136, doi:http://dx.doi.org/10.1149/1.3625232.

[51] F. Single, B. Horstmann, A. Latz, Dynamics and morphology of solid electrolyte interphase (SEI), Phys. Chem. Chem. Phys. 18 (27) (2016) 17810–17814, doi:http://dx.doi.org/10.1039/c6cp02816k.

[52] M. Lewerenz, A. Marongiu, A. Warnecke, D.U. Sauer, Differential voltage analysis as a tool for analyzing inhomogeneous aging: a case study for LiFePO$_4$-graphite cylindrical cells, J. Power Sources 368 (2017) 57–67, doi:http://dx.doi.org/10.1016/j.jpowsour.2017.09.059.